Vertical 2-μm Heterodyne Differential Absorption Lidar Measurements of Mean CO2 Mixing Ratio in the Troposphere

Fabien Gibert, Pierre H. Flamant, Juan Cuesta, Didier Bruneau

Vertical 2-μm Heterodyne Differential Absorption Lidar Measurements of Mean CO_2 Mixing Ratio in the Troposphere

FABIEN GIBERT,* PIERRE H. FLAMANT, AND JUAN CUESTA

Laboratoire de Météorologie Dynamique, École Polytechnique, Institut Pierre-Simon Laplace, Palaiseau, France

DIDIER BRUNEAU

Service d'Aéronomie, Université Pierre et Marie Curie, Institut Pierre-Simon Laplace, Paris, France

(Manuscript received 26 September 2007, in final form 14 January 2008)

ABSTRACT

Vertical mean CO_2 mixing ratio measurements are reported in the atmospheric boundary layer (ABL) and in the lower free troposphere (FT), using a 2-μm heterodyne differential absorption lidar (HDIAL). The mean CO_2 mixing ratio in the ABL is determined using 1) aerosol backscatter signal and a mean derivative of the increasing optical depth as a function of altitude and 2) optical depth measurements from cloud target returns. For a 1-km vertical long path in the ABL, 2% measurement precision with a time resolution of 30 min is demonstrated for the retrieved mean CO_2 absorption. Spectroscopic calculations are reported in details using new spectroscopic data in the 2-μm domain and the outputs of the fifth-generation Pennsylvania State University–National Center for Atmospheric Research Mesoscale Model (MM5). Then, using both aerosols in the ABL and midaltitude dense clouds in the free troposphere, preliminary HDIAL measurements of mean CO_2 mixing ratio in the free troposphere are also presented. The 2-μm HDIAL vertical measurements are compared to ground-based and airborne in situ CO_2 mixing ratio measurements and discussed with the atmospheric synoptic conditions.

1. Introduction

The importance of atmospheric carbon dioxide (CO_2) as a key contributor to greenhouse effect and so to global warming and climate change is widely documented by the scientific community (Houghton et al. 2001). In this respect, the monitoring of atmospheric CO_2 is essential for a better understanding of CO_2 concentration time and space changes at different scales, and, consequently, for an improvement in current modeling and climate prediction.

As it stands today, the most reliable monitoring activity is conducted from the ground using in situ sensors and instrumented towers in the framework of regional networks (Conway et al. 1994; Lambert et al. 1995). In addition, airborne measurements, also using in situ sensors, complement the current ground-based networks. These airborne measurements are conducted on a regular basis in some locations or during dedicated field campaigns (Matsueda and Inoue 1996; Lloyd et al. 2001; Schmitgen et al. 2004; Bakwin et al. 2003). Nevertheless, the intrinsic limitations in space and time call for a significant improvement of the overall global observational capability. Global monitoring, ultimately from space, is foreseen as a means to quantify sources and sinks on a regional scale and to better understand the links between the various components of the carbon cycle. A vertical profile would be ideal, but a column-integrated amount or column-weighted amount is also valuable, provided that the lower troposphere contributes significantly.

In the recent years, this issue led to several innovative initiatives at the international level with the Orbiting Carbon Observatory (OCO; Crisp et al. 2004) and Greenhouse Gases Observing Satellite (GOSAT; Inoue 2005) projects in the United States and Japan, re-

* Current affiliation: Department of Meteorology, The Pennsylvania State University, University Park, Pennsylvania.

Corresponding author address: Fabien Gibert, Department of Meteorology, The Pennsylvania State University, 415 Walker Building, University Park, PA 16802.
E-mail: fabien.gibert@meteo.psu.edu

DOI: 10.1175/2008JTECHA1070.1

spectively. Both projects are based on passive remote sensing techniques with great potential but inherent restrictions with respect to a demanded accuracy of 1–3 ppm (0.3%–1%) on the CO_2 total column content and significant information into the atmospheric boundary layer (ABL) to characterize surface fluxes (Rayner and O'Brien 2001).

Active remote sensors like lidar can complement the existing ground-based network and could ultimately be operated in space (Flamant et al. 2005). However, a necessary step prior to any deployment in space for global coverage measurements is a convincing demonstration of the capability of the CO_2 differential absorption lidar (DIAL) either from the ground or an aircraft platform. Preliminary ground-based measurements with a 2-μm heterodyne DIAL (HDIAL) have been reported (Koch et al. 2004; Gibert et al. 2006). CO_2 measurements in absolute value with accuracy of 1% have already been demonstrated using range-distributed aerosol targets in the ABL (Gibert et al. 2006). At the time, the HDIAL measurements were conducted looking horizontally in the ABL, which results in a simpler experimental condition with no range dependence of air density and CO_2 absorption line cross section on atmospheric variables (humidity, temperature, and pressure).

New experimental studies are necessary to assess the full potential of the DIAL technique. In this respect, the present paper addresses the first remote measurements of the vertical profile of atmospheric CO_2 mixing ratio, showing mean measurements both in the ABL and the free troposphere. Recent work by Stephens et al. (2007) has shown the importance of measurements of the vertical profile of CO_2 for constraining the global distribution of sources and sinks of CO_2. Mean spatial CO_2 mixing ratio measurements are also well suited to be directly assimilated in a transport model (characterized by a certain grid size) in order to infer regional surface fluxes. In addition, measurements of the temporal evolution of CO_2 in the ABL and in the free troposphere in conjunction with a precise knowledge of the change in ABL height that can also be observed using lidar enable one to infer diurnal and seasonal fluxes of CO_2 at a more local scale using ABL budget methods (Gibert et al. 2007c; Wang et al. 2007).

Since an intrinsic limitation to vertical HDIAL measurement is the scattering and content of aerosols (usually negligible in the free troposphere), we also propose to use dense clouds as diffuse target to make CO_2 total column-content measurements from the ground. Also, because airborne or spaceborne DIAL applications rely on surface returns, it also offers an opportunity to test the target technique for clouds, similar to other natural surfaces in terms of reflectance and small-scale correlation properties.

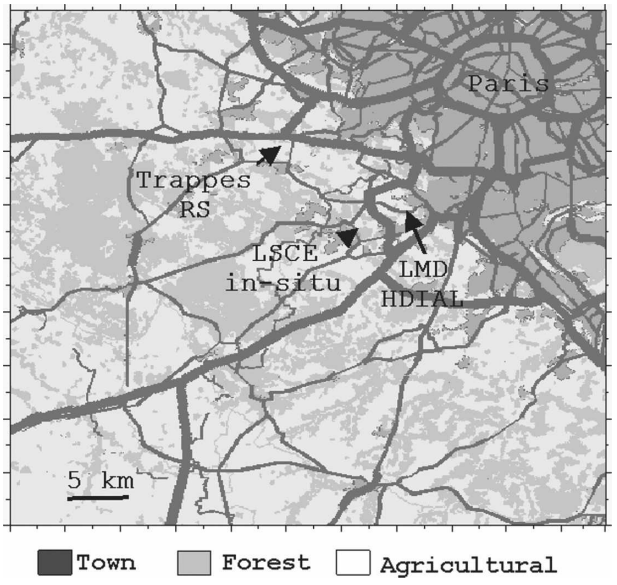

FIG. 1. Overview of the southwest Paris area where CO_2 measurements were conducted using a 2-μm HDIAL at LMD/IPSL and in situ measurements at LSCE/IPSL. Radiosoundings are launched twice daily at the meteorological station in Trappes.

Section 2 presents the overall experimental setup, that is, the HDIAL and in situ measurements. The HDIAL technique based on range-distributed aerosols target on the one hand and cloud target on the other hand is presented in section 3. In section 4, vertical HDIAL measurements of CO_2 in the ABL using aerosol backscatter signal are discussed. The DIAL technique using dense clouds is presented in section 5. Also, this section presents a direct comparison of simultaneous CO_2 mixing ratio retrievals using the two proposed techniques: cloud target and aerosol-distributed target, when cumulus clouds are present at the top of the ABL. Preliminary vertical measurements in the free troposphere are presented in the case of midaltitude clouds at 4 km in section 6.

2. Experimental setup

The 2-μm HDIAL system was operated from the Laboratoire de Météorologie Dynamique/L'Institut Pierre-Simon Laplace (LMD/IPSL) facility at the École Polytechnique located ~20 km southwest of Paris (Fig. 1). In situ routine measurements of CO_2 were conducted at Laboratoire des Sciences du Climat et de l'Environnement (LSCE)/IPSL located 5 km away from École Polytechnique. Radiosondes were launched twice a day at the nearby operational meteorological station in Trappes.

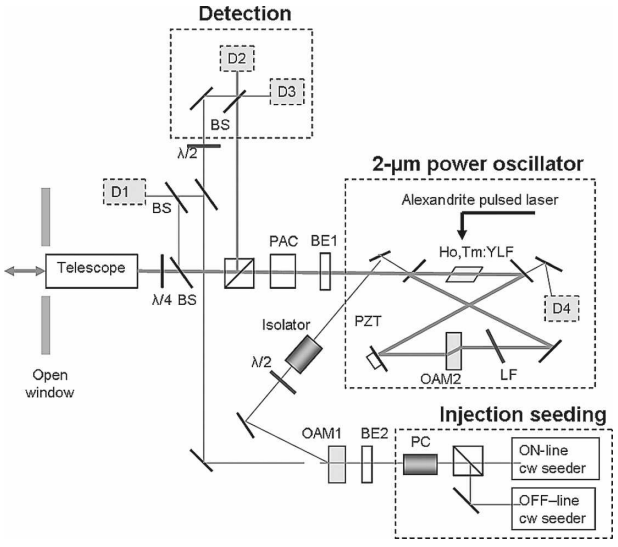

FIG. 2. Optical block diagram of the 2.06-μm HDIAL. BS: beam splitter; LF: Lyot filter; BE: beam expander; PC: Pockels cell. D1–D4 are InGaAs photodiodes.

TABLE 1. HDIAL system parameters.

Emitter laser	
Laser material	Tm, Ho:YLF
Wavelength: online/offline	2064.41/2064.10 nm
Pulse energy	10 mJ
Pulse repetition rate for a wavelength pair on–off	5 Hz
Pulse width (HWHM)	230 ns
Line width (HWHM)	2.5 MHz
LO/Seeder laser	
On- and offline continuous wave laser Tm, Ho:YLF	10 mW single mode
Heterodyne detection	
Telescope diameter	100 mm
Beat frequency between LO and atmospheric signal	25 MHz
Detection bandwidth	50 MHz
Lidar signal digitization	8 bits/125 MHz
Signal processing estimator	Levin-like filter (4-MHz bandwidth)
	Squarer

a. The 2-μm heterodyne DIAL system

The HDIAL combines 3 major capabilities: 1) CO_2 mixing ratio, 2) ABL and cloud structure, and 3) velocity measurements. The HDIAL system is based on a single-mode power oscillator (PO) in a ring cavity arrangement (Fig. 2). The PO, using a Ho, Tm: yttrium lithium fluoride (YLF) rod as an active material (Tm:5%, Ho:0.5%), is longitudinally pumped by a flashlamp-pumped 500 mJ–75 μs–10 Hz Alexandrite laser. The PO delivers 10 mJ per pulses at 10 Hz which corresponds to a 5-Hz on- and offline pair repetition rate. The On and off wavelengths are tuned alternatively by injection seeding from two continuous wave (CW) laser emitting at 2064.41 nm (online) and 2064.10 nm (offline), respectively. Because the same PO is used for the on- and offline emissions there is no trade-off optimization on the transmitted energies at the two wavelengths (Bruneau et al. 2006). A Pockels cell synchronized at a 10-Hz pulse repetition frequency with the Alexandrite laser trigger drives the injection seeding at the two wavelengths. The CW laser frequency (on and off) is matched with the PO ring cavity using the ramp and fire technique; that is, the PO ring cavity is swept when the laser gain is maximum until a resonance is detected that triggers the internal optoacoustic modulator (OAM2; Henderson et al. 1986). The intermediate frequency between the local oscillators (LO) and the PO is fixed by OAM1; the jitter is ± 1 MHz (Bruneau et al. 1997). The PO has a pulse duration of 230 ns and the resulting 2.5-MHz line width is nearly transformed limited that is suited for accurate velocity measurements. The two CW laser seeders are also used as local oscillators for heterodyne detection after a 25-MHz shifting by OAM1. Each LO enables us to reach shot-noise-limited detection. Table 1 summarizes the main 2-μm HDIAL parameters. A photo acoustic cell (PAC) filled with CO_2 at 1000 hPa is used to monitor and correct for online spectral drifts during the course of the measurements (Gibert et al. 2006, 2007b). The output beam is sent into the atmosphere through a 10-cm-diameter telescope that is pointing to an open window. An outside mirror enables vertical or slant pointing.

After collection by the same telescope, the backscattered light is mixed with the LO onto two indium–gallium–arsenide (InGaAs) detectors set in a balanced configuration for low detection noise. The detection bandwidth is limited to 50 MHz. The radiofrequency signals are analog-to-digital (AD) converted and digitized on 8 bits at a 125-MHz sampling frequency. Finally, the digital signals are stored in a PC and later processed by software developed in MATLAB programming language. The on- and offline signals are recorded simultaneously with their corresponding PAC signal. The PAC signals are normalized to the transmitted pulse energy using the reference detector (D1 on Fig. 2). A Levin-like filter is used for estimating both backscattered power and Doppler frequency (Rye and Hardesty 1993, 1997). Reference signals, that is, the outgoing on- and offline pulses are photomixed with the corresponding LO that enables us to discard outliers with frequency shift larger than 1 MHz or energy variation larger than 25%. Datasets with more than 50% rejection according to the criteria on frequency

shift and energy variation above are discarded (it corresponds to a relax mode of the PO). The HDIAL range resolution is 75 m corresponding to the processing range gate. When pointing at zenith, the HDIAL useful signals start at the third range gate or about 200 m above the surface. In most practical condition, the ABL aerosol loading enables 2-μm HDIAL measurements up to the top of the convective ABL. In contrast, a low aerosol content in the free troposphere prevents CO_2 measurements. This inherent limitation is the motivation for a new study to demonstrate the possibility to measure CO_2 column content using dense clouds.

b. In situ measurements

In addition to meteorological information provided by radiosounding, two sets of in situ data are collected at LMD/IPSL and LSCE/IPSL. In situ sensors implemented on the building roof at École Polytechnique (12 m above the ground) provide time series of temperature, pressure, relative humidity, and wind direction. In Saclay (LSCE/IPSL) an automated gas chromatographic system (HP-6890) has been operated since September 2000 for ambient air composition, that is, CO_2, CH_4, N_2O, and SF_6 in flask samples (for high accuracy) and in routine continuous measurements reported every 5 or 15 min depending on the sampling procedure. The standard accuracy is 0.5 ppm (Worthy et al. 1998; Pépin et al. 2002). In addition, airborne measurements in the free troposphere are conducted every 2 weeks by LSCE/IPSL using a commercial infrared absorption analyzer (from Li-Cor, Inc., model 6262) on board a light aircraft. It takes off from an airfield located near Saclay and Palaiseau and it flies to Orleans, 100 km south of Paris.

3. Theoretical considerations

The heterodyne signal consists in ac radio frequency (RF) voltage. For on and off wavelength (index i) the HDIAL signal is

$$S_i(t) \propto \gamma_i \sqrt{P_i(t) P_{\mathrm{LO},i}(t)} \exp[j(2\pi \upsilon_{H,i} t + \varphi_i)], \quad (1)$$

where γ_i is the heterodyne efficiency ($0 \le \gamma_i \le 1$), P_i is the atmospheric scattered power collected by the receiver telescope, and $P_{\mathrm{LO},i}$ is the LO power. Here, the RF $\upsilon_{H,i}$ is the difference between the on (or off) return signal frequency including a Doppler frequency shift ($\pm\Delta\upsilon_D$) due to aerosol particles in motion, and on (or off) LO frequency; that is, $\upsilon_{H,i} = 25 \pm \Delta\upsilon_D$.

The atmospheric signals are accumulated in the range gate of 75 m (ΔR) or 0.5-μs duration ($\Delta t = 2\Delta R/c$, c being the light velocity) along the line of sight that results in mean scattered power at the two frequencies at range R: $\langle P_{\mathrm{Off}}(R)\rangle = \langle |S_{\mathrm{Off}}(t)|^2\rangle$ and $\langle P_{\mathrm{On}}(R)\rangle = \langle |S_{\mathrm{On}}(t)|^2\rangle$.

a. Definitions: CNR and SNR

The carrier-to-noise ratio (CNR) is given by

$$\mathrm{CNR}_i = \frac{\overline{\langle P_i \rangle}}{\overline{\langle P_{B,i} \rangle}}, \quad (2)$$

where $\overline{\langle P_i \rangle}$ and $\overline{\langle P_{B,i} \rangle}$ are the mean signal and mean noise power estimate in a range gate after M_p shots averaging for the i line, respectively, for a range z set in the middle of the range gate. Both squarer and modified Levin estimators are used as a double check to calculate $\overline{\langle P_i \rangle}$ (Rye and Hardesty 1993, 1997).

Theoretical on- and offline signal-to-noise ratio ($\mathrm{SNR}_i = \overline{\langle P_i \rangle}/\sigma(\langle P_i \rangle)$) can be calculated for the squarer estimator using an analytical expression from Rye and Hardesty (1997) and experimental CNR:

$$\frac{1}{\mathrm{SNR}_{i,\mathrm{squarer}}} = \frac{1}{\sqrt{M_p M_t}} \left(1 + \frac{1}{\mathrm{CNR}_i}\right), \quad (3)$$

where $\mathrm{SNR}_{i,\mathrm{squarer}}$ accounts for speckle and detection noise and $M_t = \sqrt{1 + (\delta t_R/T_c)^2}$ is the number of coherence cells in a range gate, assuming a Gaussian pulse of duration T_c and a rectangular range gate of duration δt_R. The experimental value, for distributed aerosol target, is $M_t \approx 6$, whereas the calculated value amounts to 4.5 using $T_c = 230$ ns and $\delta t_R = 1$ μs.

The squarer estimate of SNR from CNR measurements ($\mathrm{SNR}_{\mathrm{squarer}}$) enable us to predict the theoretical HDIAL instrument performances even though it does not take into account the standard deviation of $\overline{\langle P_i \rangle}$ according to changes in atmospheric aerosol scattering variability.

On the contrary, the experimental signal-to-noise ratio SNR_i, calculated from a modified Levin estimate of the return power at each wavelength, takes into account the total standard deviation of $\overline{\langle P_i \rangle}$ for speckle and detection noises and atmospheric aerosol backscattering variability. It is used to estimate the error on optical depth estimates.

b. CO_2 mixing ratio measurement

Considering the simplified lidar equation, the atmospheric scattered power in a range gate ΔR at range R is

$$\langle P_i(R)\rangle = \frac{K_i}{R^2} E_i \langle \gamma_i(R)\rangle \langle \beta_i(R)\rangle \exp\left[-2\int_0^R (\alpha_i(r) + \alpha_{\beta,i}(r))\, dr\right], \quad (4)$$

where K_i is a instrumental constant for the wavelength i, E_i is the pulse energy, γ_i is the heterodyne efficiency, β_i is the elastic backscatter coefficient ($m\ sr^{-1}$), α_i is the CO_2 absorption (m^{-1}), and $\alpha_{\beta,i}$ is the extinction coefficient (m^{-1}).

1) Optical depth

Assuming that the on and off lines are close enough to neglect aerosol backscattering and extinction variations with wavelength (appendix A), the optical depth due to CO_2 absorption between two altitudes 0 and z is expressed as (Remsberg and Gordley 1978; Megie and Menzies 1980)

$$\tau(0, z) = \frac{1}{2} \ln\left[\frac{\overline{\langle P_{\mathrm{Off}}(z)\rangle}}{\overline{\langle P_{\mathrm{On}}(z)\rangle}}\right], \tag{5}$$

where $\overline{\langle P_{\mathrm{Off}}(r)\rangle}$ and $\overline{\langle P_{\mathrm{On}}(r)\rangle}$ are the mean off- and online received powers in a range gate normalized by energy pulse and heterodyne efficiency after M_p shots averaging.

Using spectroscopic data, (5) is written as

$$\tau(0, z) = \int_0^z \rho_{\mathrm{CO}_2}(r) n_a(r)[\tilde{\sigma}_{\mathrm{On}}(r) - \tilde{\sigma}_{\mathrm{Off}}(r)]\, dr, \tag{6}$$

where $\rho_{\mathrm{CO}_2}(z)$ is the CO_2 mixing ratio, $\tilde{\sigma}_{\mathrm{On}}$ and $\tilde{\sigma}_{\mathrm{Off}}$ are the on- and offline effective absorption cross sections (accounting for spectral shift as recorded by the PAC; see section 4), and $n_a(z)$ is the dry-air density:

$$n_a(z) = \frac{p(z)}{kT(z)} \frac{1}{1 + \rho_w(z)}, \tag{7}$$

where ρ_w is the water vapor mixing ratio, p is the pressure, T is the temperature, and k is the Boltzmann constant.

2) CO_2 mixing ratio measurement using the slope method in the ABL

From (6), (7), and using $\Delta\tilde{\sigma}(z) = \tilde{\sigma}_{\mathrm{on}}(z) - \tilde{\sigma}_{\mathrm{off}}(z)$ it comes

$$\rho_{\mathrm{CO}_2}(z) = \frac{1}{\mathrm{WF}(z)} \frac{d\tau(0, z)}{dz}, \tag{8}$$

where $\mathrm{WF}(z) = n_a(z)\, \Delta\tilde{\sigma}(z)$ is a weighting function.

The error reduction on the CO_2 mixing ratio requires an averaging over several range gates. A fruitful approach, called the "slope method," consists in calculating a mean CO_2 differential absorption coefficient ($\alpha = d\tau/dz$) as the slope of the cumulative optical depth as a function of range. In practice, α is obtained by a mean-square least fit of the optical depth (accounting for standard deviation) as a function of range (Gibert et al. 2006).

TABLE 2. Spectroscopic data for the CO_2 online of interest. Here S_0 is the line strength at 296 K, γ_0 is the collision half-width, E'' is the energy of the lower level of the transition, and t is the coefficient for a temperature dependence of the collision half-width. Data marked * are from Regalia-Jarlot et al. (2006) with 2% accuracy, and data marked ** are from the HITRAN database (Rothman et al. 1998) with 10% accuracy.

Λ (nm)	S_0 (cm mole c^{-1})	γ_0 (cm^{-1} atm^{-1})	E'' (cm^{-1})	t
2064.41	2.35×10^{-22}*	0.077**	6087.0**	0.69**

3) CO_2 mixing ratio measurement in the free troposphere using midaltitude clouds

The CO_2 mixing ratio in the free troposphere is retrieved by taking the difference between the total path-integrated CO_2 measurement to the cloud base and the slope method in the ABL. To derive the mean CO_2 mixing ratio in the free troposphere $\bar{\rho}_{\mathrm{CO}_2}$, t, the path-integrated optical depth to the cloud base is divided in two parts as follows:

$$\tau(0, z_c) = \mathrm{SWF}_a \bar{\rho}_{\mathrm{CO}_2, a} + \mathrm{SWF}_t \bar{\rho}_{\mathrm{CO}_2, t}, \tag{9}$$

where $\bar{\rho}_{\mathrm{CO}_2}$, a is the mean CO_2 mixing ratio in the ABL, z_a and z_c are the ABL and midcloud altitude, and $\mathrm{SWF}_a = \int_0^{z_a} \mathrm{WF}(r)\, dr$ and $\mathrm{SWF}_t = \int_{z_a}^{z_c} \mathrm{WF}(r)\, dr$ are the integrated weighting functions in the ABL and in the free troposphere, respectively. From (9) it comes

$$\bar{\rho}_{\mathrm{CO}_2, t} = \frac{\tau(0, z_c) - (\mathrm{SWF}_a \bar{\rho}_{\mathrm{CO}_2, a})}{\mathrm{SWF}_t}. \tag{10}$$

c. *Spectroscopic data and weighting function (WF)*

In the present study, we use new data for the line strength of the CO_2 P12 line at 2064.41 nm as provided by a recent experimental study (Regalia-Jarlot et al. 2006). The discrepancies with the high-resolution transmission (HITRAN) database amount to 10%. In the absence of new data on line width and exponent for temperature dependence, we used the information provided in the HITRAN database (see Table 2; Rothman et al. 1998).

The weighting function $\mathrm{WF}(z)$ is computed using vertical profiles of temperature, pressure, and specific hu-

midity from fifth-generation Pennsylvania State University–National Center for Atmospheric Research Mesoscale Model (MM5) analysis (Grell et al. 1995). The time resolution is one hour. Also, the same WF(z) has been computed using radiosounding when available.

d. Error analysis on CO_2 HDIAL measurements

1) Statistical error on optical depth measurement

The relative error on optical depth measurement is (Killinger and Menyuk 1981)

$$\frac{\sigma(\tau)}{\tau} = \frac{1}{2\tau}\sqrt{\frac{1}{\mathrm{SNR}_{\mathrm{Off}}^2} + \frac{1}{\mathrm{SNR}_{\mathrm{On}}^2} - 2\frac{\rho(\overline{\langle P_{\mathrm{On}}\rangle}, \overline{\langle P_{\mathrm{Off}}\rangle})}{\mathrm{SNR}_{\mathrm{Off}}\mathrm{SNR}_{\mathrm{On}}}}, \tag{11a}$$

where $\mathrm{SNR}_{\mathrm{On}} = \overline{\langle P_{\mathrm{On}}\rangle}/\sigma(\langle P_{\mathrm{On}}\rangle)$ and $\mathrm{SNR}_{\mathrm{Off}} = \overline{\langle P_{\mathrm{Off}}\rangle}/\sigma(\langle P_{\mathrm{Off}}\rangle)$ are the on- and offline signal-to-noise ratios, respectively; $\sigma(\langle P_{\mathrm{On}}\rangle)$ and $\sigma(\langle P_{\mathrm{Off}}\rangle)$ are the measured standard deviation on atmospheric backscattered signals accounting for speckle noise, detection noise, and atmospheric aerosol backscatter variability; $\rho(\overline{\langle P_{\mathrm{On}}\rangle}, \overline{\langle P_{\mathrm{Off}}\rangle})$ is the cross-correlation coefficient. This parameter is quite difficult to estimate in practice. Therefore, in the present study, we chose to overestimate the relative error on the optical depth by setting $\rho(\overline{\langle P_{\mathrm{On}}\rangle}, \overline{\langle P_{\mathrm{Off}}\rangle}) = 0$. Then (11a) reduces to

$$\frac{\sigma(\tau)}{\tau} \cong \frac{1}{2\tau}\sqrt{\frac{1}{\mathrm{SNR}_{\mathrm{Off}}^2} + \frac{1}{\mathrm{SNR}_{\mathrm{On}}^2}}. \tag{11b}$$

Also, it can be shown (appendix C) that the bias on optical depth estimate is given by

$$\frac{\delta(\tau)}{\tau} \cong \frac{1}{4\tau}\sqrt{\frac{1}{\mathrm{SNR}_{\mathrm{On}}^2} - \frac{1}{\mathrm{SNR}_{\mathrm{Off}}^2}}. \tag{12}$$

We choose to systematically correct our optical depth measurements using Eq. (12).

2) Error on HDIAL measurement using aerosol target in the ABL

For normally distributed noise, the least square fit used to determine the mean CO_2 differential absorption coefficient, α, corresponds to a maximum likelihood estimate. The accuracy on α depends on 1) the maximum range that is limited to the ABL height at best and 2) the standard deviation on individual optical depth measurements. The accuracy can be further improved by averaging. Therefore, the HDIAL measurement error is given by

$$\frac{\sigma(\rho_{\mathrm{CO}_2,a})}{\rho_{\mathrm{CO}_2,a}} = \sqrt{\left[\frac{\sigma(d\tau/dr)}{d\tau/dr}\right]^2 + \left[\frac{\sigma(\mathrm{WF})}{\mathrm{WF}}\right]^2}. \tag{13}$$

3) Error on HDIAL CO_2 measurement using midaltitude cloud reflectivity

Using (8) and (9), the total error including statistical and spectroscopic error is given by

$$\sigma(\bar{\rho}_{\mathrm{CO}_2,t}) = \sqrt{\left[\frac{\tau(0,z_c)}{\mathrm{SWF}_t}\right]^2\left(\left\{\frac{\sigma[\tau(0,z_c)]}{\tau(0,z_c)}\right\}^2 + \left[\frac{\sigma(\Delta\tilde{\sigma})}{\Delta\tilde{\sigma}}\right]^2\right) + \left[\sigma(\bar{\rho}_{\mathrm{CO}_2,a})\frac{\mathrm{SWF}_a}{\mathrm{SWF}_t}\right]^2}. \tag{14}$$

4. The 2-μm HDIAL technique using range-distributed aerosol target

On 10 June 2005 (J10 case), the HDIAL measurements started first horizontally at 0430 UTC for 20 min. Then vertical measurements were made at 0730 UTC.

a. Meteorological conditions

Ground-based meteorological data measured at LMD/IPSL are displayed in Fig. 3. The sunrise occurred at 0430 UTC. A mean ~3 m s^{-1} northeast wind brought an air mass from the Paris urban area. Figure 4 displays the vertical HDIAL measurements for offline backscatter signal and vertical velocity. The ABL starts to rise at 0830 UTC. After 0900 UTC, strong up- and downdrafts are seen (Fig. 4b), which enables us to identify the mixed layer. The ABL top reached 2000 m after 1430 UTC and cumulus clouds appeared after 1300 UTC. After the sunset at 2000 UTC, vertical velocities up to ±0.5 m s^{-1} [the typical noise level for HDIAL velocity measurement is less than 0.2 m s^{-1} for 600 shots averaged (Bruneau et al. 2000)] are still observed, which indicates that a vertical mixing remained during the night.

Figure 5 displays the potential temperature and the calculated weighting function, WF, from MM5 analysis. Before 0900 UTC, WF vertical structure reflects the temperature inversion with height [Eq. (B10) in appendix B]. The top of the nocturnal layer (NL) is identified at ~300 m from the temperature inversion. After the rise of the ABL, WF increases with z according to a corresponding decrease in temperature (Fig. 5). After 1800 UTC, both $\theta(z)$ and WF(z) vertical profiles keep the same variations as in the midafternoon, which indi-

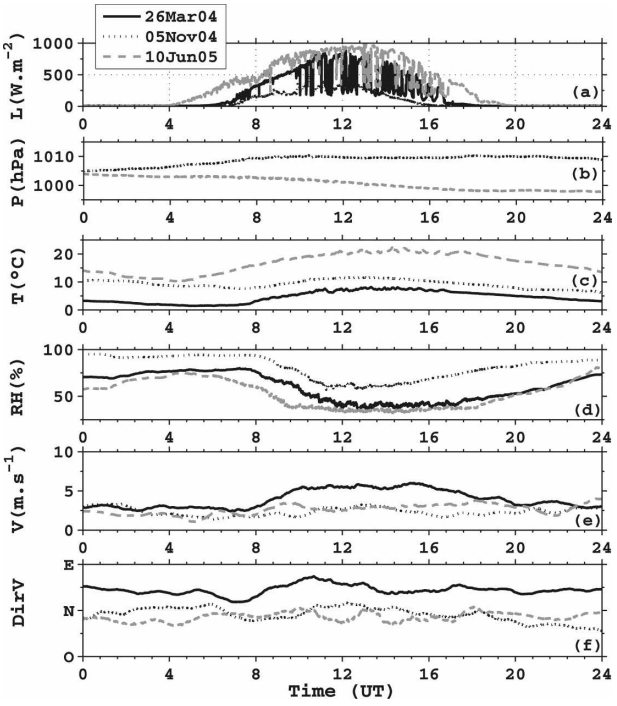

FIG. 3. Time series of in situ sensors measurements at 10 m above ground at LMD/IPSL on the three days analyzed in the present paper (a) shortwave radiation, (b) pressure (there was no sensor before April 2004), (c) air temperature, (d) relative humidity, (e) mean horizontal wind velocity (1-h averaged data), and (f) mean horizontal wind direction (1-h averaged data).

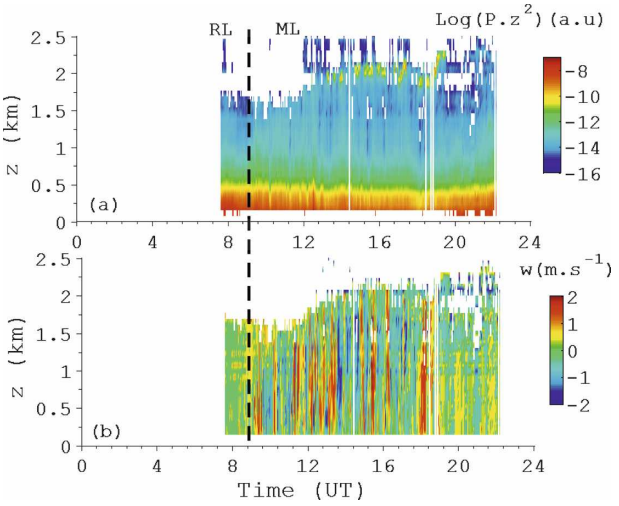

FIG. 4. 10 Jun 2005. Time–height color plots of (a) offline backscatter signal and (b) vertical velocity measured by HDIAL. In (a) color plot is for $\ln(\langle P \rangle z^2)$ in arbitrary unit (red is for the strongest return signals). In (b) positive velocity (red) is upward. Range and time resolution are, respectively, 75 m and 2 min. Solar time is UTC time and local time is UTC time + 2 h.

cates that the ABL is weakly vertically stratified. This result is in good agreement with the observed vertical velocities (Fig. 4b).

b. HDIAL instrument performances

Figure 6a displays the on- and offline CNRs for a 2-min time averaging ($M_{p,i}$ = 600 shots) at 1100 UTC. The CNRs decrease rapidly with altitude accordingly to a strong decrease of aerosol concentration. In practice, it sets a limit on range for the HDIAL measurements to about 1.2 km, while the ABL height reached 2 km in the midafternoon. Figure 6b shows the cumulative optical depth as a function of range and the mean-square least fit used to calculate the CO_2 absorption coefficient α. The measured (modified Levin estimator) and calculated (CNR and squarer estimator) standard deviation of return power are used to compare measured and calculated relative errors on optical depth (Fig. 6c). The lower optical depth relative error amounts to ~4% for 600 shot pairs averaged at an altitude of 0.6 km. A weak CNR_{on} at ~1.2 km entails a large increase of optical depth error (Figs. 6b,c). Measured standard deviations (Levin estimator) and calculated ones [from Eqs. (3) and (11b) and squarer estimator] are in good agreement. For the weak online CNRs (CNR < −10 dB) the modified Levin estimator obtains the best results as expected (Rye and Hardesty 1997). We estimated the digitizing noise associated to the 8-bit–125-MHz digitizer (appendix D). Figure 6c shows that the impact of such a digitizer on the measurements is negligible. In the same way, the potential optical depth errors induced by the spectral dependence of aerosols optical properties are also negligible (see appendix A and Table 3).

c. Mean CO_2 mixing ratio measurements in the ABL

The calculated slopes before (i.e., α) and after the PAC correction (i.e., $\alpha WF_0/WF$) are displayed on Fig. 7b. Here WF_0 is the calculated weighting function at line center and WF accounts for some detuning from line center. The PAC unit enables us to measure the spectral shift of the online emission with respect to the center of the P12 CO_2 absorption line, and therefore to make an a posteriori correction of the effective CO_2 cross section during the course of the measurements (Fig. 7a). The HDIAL system was quite unstable after 1200 UTC partly because of large temperature fluctuations in the room (note that the window is open during the measurements). The corresponding statistical errors are shown in Fig. 7c. When the optical depth is small, that is, associated to significant online detuning from line center, CNR_{On} increases at long range and the error on optical depth $\sigma(\tau)$ decreases. However, the relative error $\sigma(\tau)/\tau$ increases (see Fig. 7c) according to

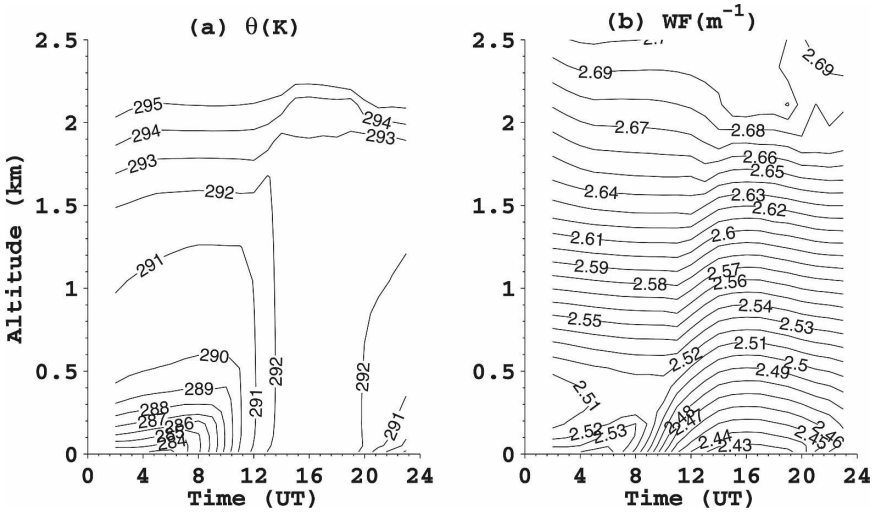

FIG. 5. 10 Jun 2005. Time series of (a) the potential temperature profiles θ (K) from MM5 analysis and (b) calculated weighting function profiles WF (m^{-1}) using spectroscopic data from Table 2 and MM5 outputs for temperature, pressure, and specific humidity. Solar time is UTC time and local time is UTC time + 2 h.

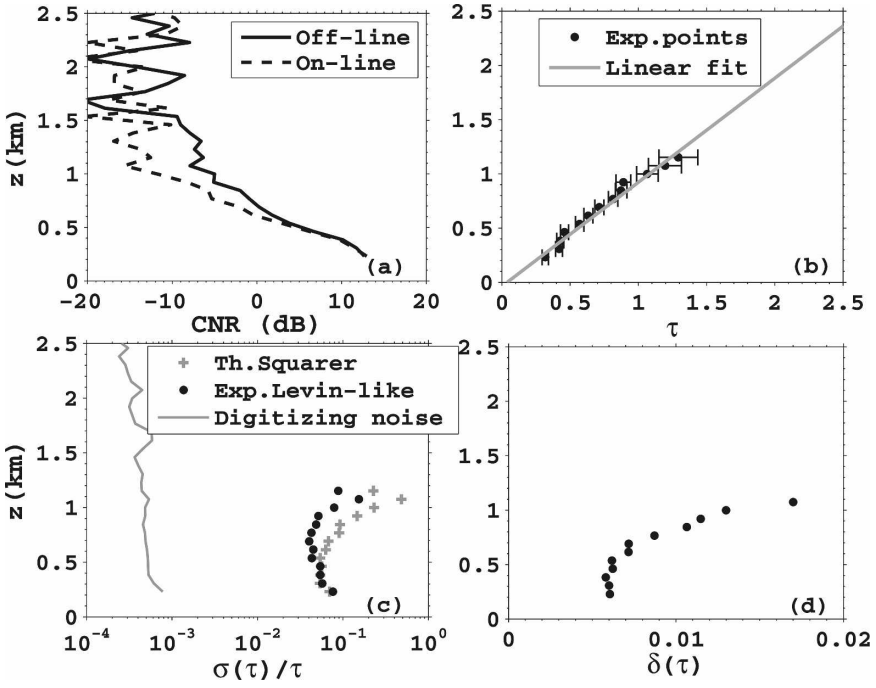

FIG. 6. HDIAL measurements on 10 Jun 2005 at 1100 UTC. (a) Online (dashed curve) and offline (solid curve) CNRs as a function of altitude for 600-shot-pair averaging (2 min) and 75-m range resolution. (b) Experimental optical depth estimates corrected from statistical bias [see (d)] as a function of altitude. The mean CO_2 differential absorption is estimated between 0.2 and 1.2 km using a linear fit weighted by optical depth std dev (error bars): $\tau = \alpha.z + \varepsilon$, $\varepsilon = 0.04 \pm 0.02$, and $\alpha = 1.04 \pm 0.04$ km^{-1} as a result of a least square fit regression. (c) Relative error on measured optical depth using the Levin estimator. Theoretical error on optical depth is also calculated using a Squarer estimator and Eqs. (2), (3), and (11b). (d) Statistical bias on optical depth estimate as a function of altitude.

TABLE 3. Statistic and systematic uncertainties of vertical HDIAL mean CO_2 mixing ratio measurements in the ABL.

Parameter	Uncertainty (%)	Comment
Statistical error: α		Slope method (1-km-long path)
Random	7	2-min averaging
	2	30-min slice averaging
Corrected bias	0.1	See appendix B
Digitizing noise	<0.05	See appendix D
Scattering change with on and off wavelength		See appendix A, bias
Extinction coefficient	<0.0005	Approximation in lidar equation
Backscatter coefficient	<0.05	
Spectroscopic error: WF		See Table 2
Spectroscopic data	2	
P12 line cross section		
Meteorological data		See appendix B, random
Temperature ±1 K	0.4	Laser line located in the center of the absorption line
	<0.8	For any spectral shift from the line center
Surface pressure ±1 hPa	<0.1	
Specific humidity ± 2%	<0.2	
Laser line positioning		
Mode hopping	−0.25	Bias
Doppler shift of the backscattered laser line (<5 MHz)	<0.2	Random, possible correction using radial velocity measurements
PAC	1	Random, noise background

a previous study on DIAL optimization in heterodyne detection (Bruneau et al. 2006).

Figure 8 displays both the HDIAL and in situ CO_2 mixing ratio measurements on 10 June 2005. The temporal resolution is 2 min. The standard deviation on mean CO_2 mixing ratio is ~7% and reduces to ~2% for a 30-min sliding average, or about 7 ppm (Fig. 8 and Table 3). For the different cases analyzed in this paper, the discrepancies between MM5 and radiosounding are within ±1 K for the temperature profile, 20% for specific humidity profile and ±1 hPa for surface pressure. The resulting errors on WF are summarized in Table 3. These errors entailed a relative error on WF lower than 0.8%, whatever the spectral shift from the CO_2 P12 line center is (appendix B). Appendix B shows that the main WF error is due to the limited knowledge on the temperature profile. In addition, Eq. (B10) shows that WF and temperature variations are of opposite signs. Accuracy and precision are sufficient to observe 1) large regional- and synoptic-scale sources, sinks, and gradients in the ABL (Wang et al. 2007); 2) changes in tropospheric CO_2 associated with the passage of strong frontal boundaries (magnitude of a few to 40 ppm; Hurwitz et al. 2004); and 3) variations of the mean CO_2 mixing ratio in the ABL due to anthropogenic emissions (Idso et al. 2002; Braud et al. 2004). However, this will only marginally constrain the ABL-mean diurnal cycle in CO_2 associated with the biological cycle of daytime net photosynthesis and nighttime respiration, which is weak in amplitude (about 5 ppm at a few hundred meter altitude) above the surface layer (Bakwin et al. 1998). A 6-h average would yield 2-ppm precision. This is sufficient precision to observe the vertical differences between the ABL and the free troposphere that can be as high as several parts per million in the summer over land (e.g., Yi et al. 2004). These vertical gradients change primarily with synoptic passages and season, hence long time averages can be used to quantify the ABL − free troposphere (FT) CO_2 difference.

d. Comparison between HDIAL and ground-based in situ measurements

During summer, several factors contribute to significant CO_2 mixing ratio variations in the ABL in the Paris area: 1) traffic fuel combustion, 2) active vegetation photosynthesis and respiration, and 3) ABL diurnal cycle. During the night, the CO_2 density increases regularly while the NL is kept at a low height (few hundreds of meters) as it is observed before 0500 UTC. After 0600 UTC and until 0900 UTC the vertical HDIAL measurements are conducted in the residual layer (RL) mostly, whereas in situ measurements were still embedded in the NL (see Figs. 4, 5, 8). Accordingly, the HDIAL CO_2 density measurements are ~15 ppm lower than those measured by the ground-based in situ sensor. On this day, the CO_2 density in the RL is comparable to the values obtained later in the after-

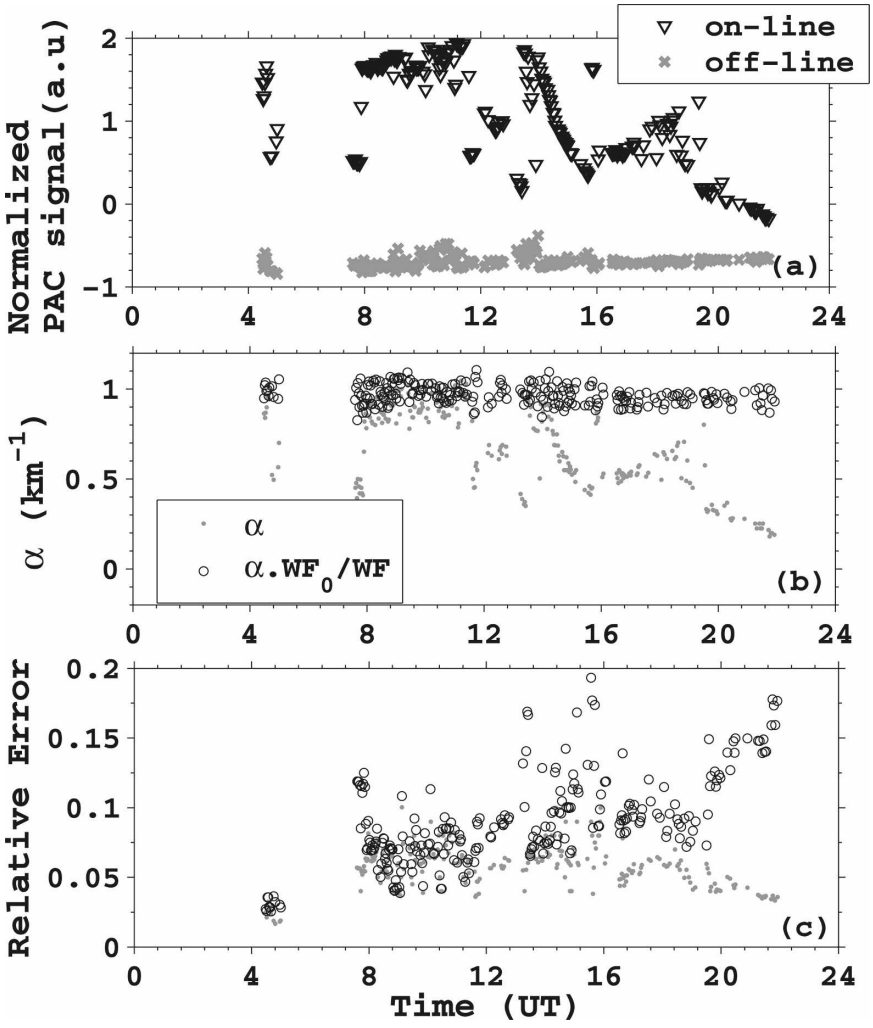

FIG. 7. Experimental results on 10 Jun 2005. (a) On- and offline PAC signals normalized by the corresponding mean pulse energy. (b) Experimental slopes ($\alpha = d\tau/dz$) or mean extinction coefficient due to CO_2 absorption (km^{-1}) as computed every 2 min (gray dots) and corrected slopes ($\alpha WF_0/WF$) using PAC signal (open circles). (c) Relative error on CO_2 absorption measurements before (gray dots) and after (open circles) PAC correction.

noon. After 0930 UTC, the HDIAL measurements at LMD/IPSL are similar to those obtained by in situ sensor at LSCE/IPSL. Figure 9 displays the National Centers for Environmental Prediction (NCEP) 1000-m-height back trajectories on 10 June 2005, for different times of the day. They show a change in wind direction coming from the northeast (over rural areas) around 0800 UTC to the north in the evening around 2000 UTC crossing the Paris area and its suburbs. Despite of the different locations between the two sites, no major differences are seen when comparing in situ and HDIAL measurements. A possible explanation is that the large vertical velocities and height of the ABL entailed a good vertical mixing and dispersion of the anthropogenic emissions from the Paris area.

In addition to the vertical measurements reported above, horizontal measurements have been made in early morning before 0600 UTC in the shallow NL (Fig. 8a). Horizontal wind information provided by in situ sensor at LMD/IPSL indicated a northwest wind direction (320°) close to the surface (Fig. 3f). The HDIAL and in situ CO_2 measurements are in good agreement for they are embedded in the same NL air mass coming from rural areas without a significant anthropogenic contribution (Fig. 1).

It is worth noting that the HDIAL instrument has the ability to provide a spatial average of CO_2 mixing ratio in the boundary layer. Therefore, it is less sensitive than an in situ sensor to the heterogeneity of the surface flux at the short scale (i.e., horizontal scale <1 km). This

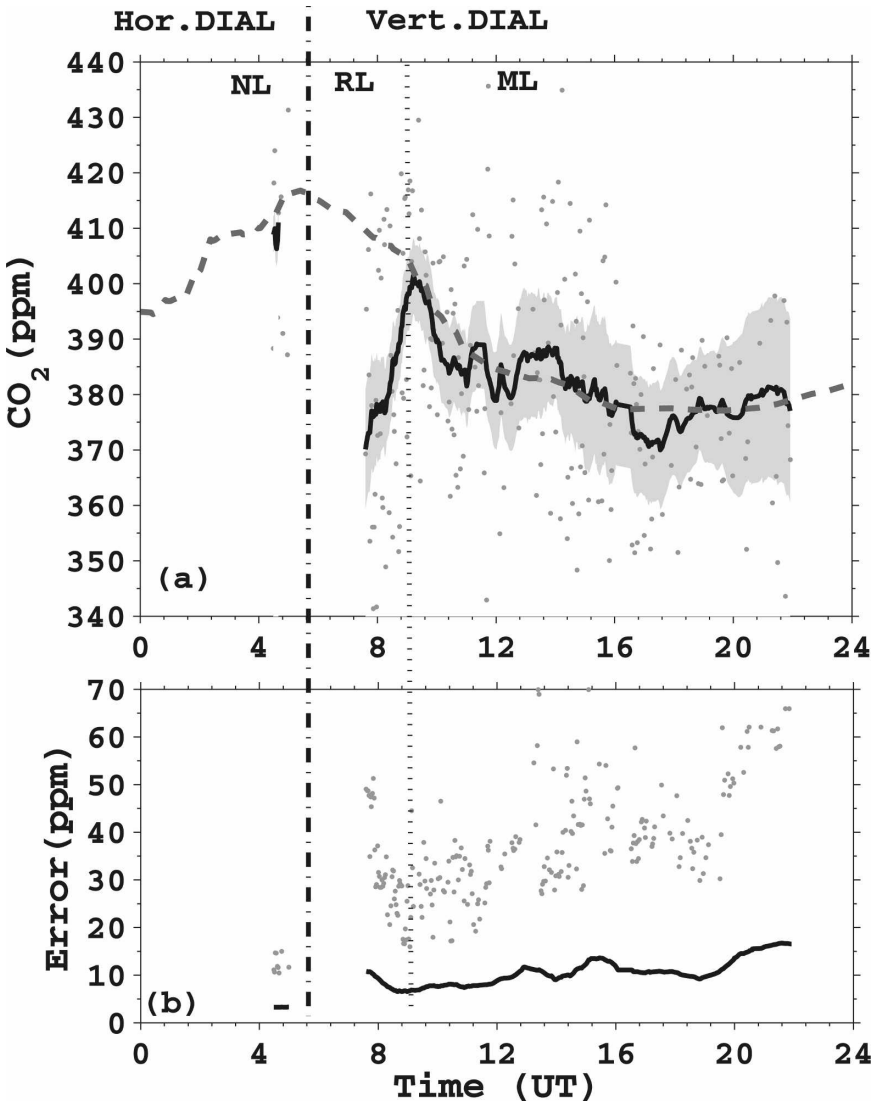

FIG. 8. Experimental results on 10 Jun 2005. (a) CO_2 mixing ratio as measured by the 2-μm HDIAL pointing vertically for 600-shot-pair averaging or 2 min (gray dots) and 15-point sliding averaging or 30-min averaging (solid line) and LSCE in situ routine measurements (dashed line). The gray area corresponds to the standard deviation on the 30-min averaged measurements. (b) Statistical relative error on HDIAL CO_2 measurements associated to the slope method for 2-min averaging (cross) and 15-point sliding or 30-min averaging (solid line). Notice that the HDIAL measurements before 0600 UTC were made pointing horizontally in the NL, whereas measurements in the RL and ML were made pointing at zenith. Solar time is UTC time and local time is UTC time + 2 h.

kind of measurement is of enormous interest for the CO_2 scientific community, which aims to infer surface fluxes from ground-based in situ CO_2 mixing ratio measurements and a transport model. The usual issue is to make an assumption that the in situ measurement has the spatial representativity of the model grid (10^3–10^4 km^2). A ground-based or airborne HDIAL system has the potential to estimate the availability of such an assumption.

5. DIAL technique using clouds as hard targets

a. The specificity of cloud target

Dense water clouds act as diffuse targets with large SNR after averaging to mitigate the shot-to-shot power fluctuations due to the speckle effect. The effective water cloud diffuse reflectance is $\rho = k_w/2\eta$, where k_w is the backscatter-to-extinction ratio at the probing wavelength, η is a multiple scattering factor that is nearly

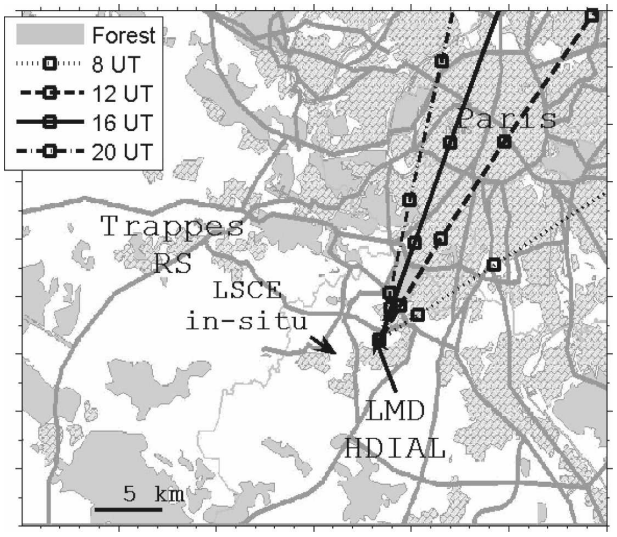

FIG. 9. 10 Jun 2005. NCEP 1000-m-height back trajectories at different times of the day. The time interval (sampling) between two squares along the same trajectory is 1 h.

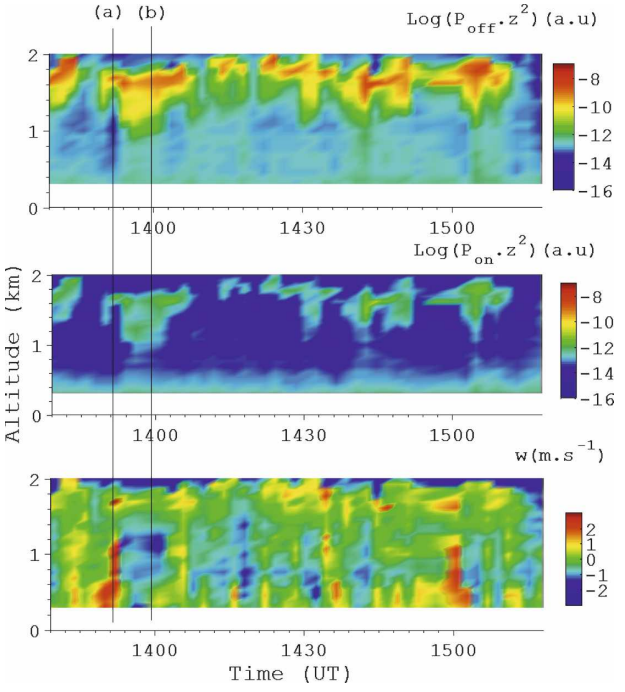

FIG. 10. Experimental results on 26 Mar 2004. Time–height color plots of (top) offline, (middle) online range-corrected backscatter signals, and (bottom) vertical velocity measured by the HDIAL. Range and time resolution are 75 m and 2 min, respectively. (a), (b) The time of optical depth profiles displayed on Figs. 11a and 11b, respectively. Solar time is UTC time and local time is UTC time + 2 h.

equal to unity in the case of a diffraction-limited system to be used for efficient heterodyne detection. Using the published data at 1.6 and 2 μm, we obtain $k_w \cong 0.04$ and $\rho \cong 2$ % (Tonna 1991).

Cloud targets do not suffer from differential reflectance problem when the on- and offline spectral interval is small, that is, the variation in index of refraction (both real and imaginary parts) is negligible. Considering the spectral interval between on- and offline, that is, 0.3 nm, we made numerical simulations using a Mie scattering code for homogeneous spherical particles and accounted for the water refractive index to simulate cloud particle properties (see appendix A). As for aerosols in the ABL, it showed that the differential backscatter and extinction coefficients between the on and off wavelengths entail a negligible error on the HDIAL CO_2 differential absorption measurement. It is not the case for topographic targets in the thermal IR at 3, 6, and 10 μm, and a differential reflectance may result in a bias on DIAL measurements (see Liou 1981).

Hard target returns result in some correlation of the on- and off-return signals that needs to be taken into account (Killinger and Menyuk 1981). Atmospheric aerosol backscatter variations correlate the on- and offline averaged signals, whereas the speckle noise results in decorrelation. Consequently, for a given time averaging, $\rho(\overline{\langle P_{on}\rangle}, \overline{\langle P_{off}\rangle})$ varies with the number of samples (or the duration of the time gate). The longer the temporal gate is, the more the signals are correlated, that is, at long time scales the atmospheric backscatter structures prevail that prevent us from calculating it properly. Further investigations will be conducted in the future to adequately address this problem. At present, we chose to overestimate the relative error on the optical depth by considering $\rho(\overline{\langle P_{on}\rangle}, \overline{\langle P_{off}\rangle}) = 0$ on cloud returns.

b. *Direct comparison of cloud target and slope method using distributed aerosol in the ABL*

To assess the performance of the HDIAL technique using cloud target for path-integrated measurements, we performed a direct comparison with the slope method. On 26 March 2004 cumulus clouds where present at the top of the boundary layer between 1330 and 1530 UTC. The two techniques, that is, cloud target and slope method, can be compared directly for the same total range. Figure 10 shows the time series of the off- and online signals, that is, $\ln(\overline{\langle P\rangle z^2})$, and vertical velocities in the convective boundary layer. The time averaging is 2 min, that is, 600 shot pairs, and the vertical resolution is 75 m. Figure 11 displays an increasing optical depth as a function of altitude at 1350 UTC (Fig. 11a) and 1405 UTC (Fig. 11b). The slope method relying on distributed aerosol is plotted as open circles with the corresponding standard deviation. The maximum

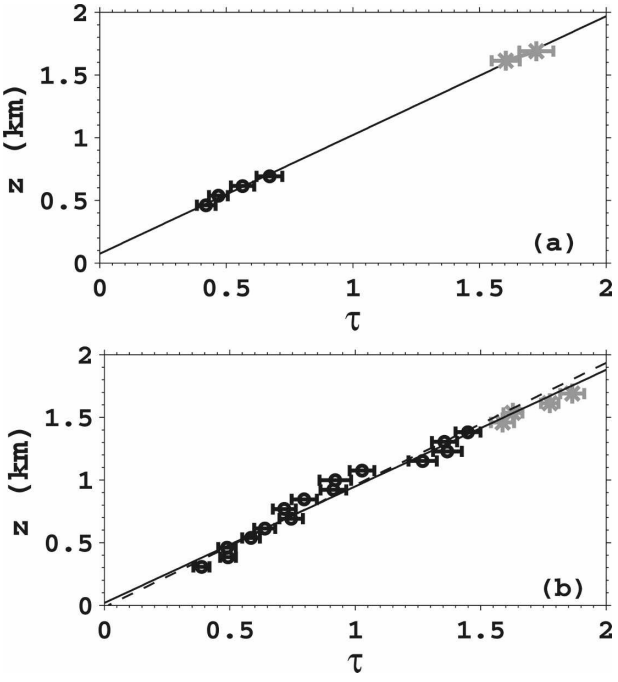

FIG. 11. Experimental results on 26 Mar 2004. Optical depth estimates using ABL aerosol targets on the one hand (○) and dense cloud returns on the other hand (*) at (a) 1350 UTC: the aerosol loading is not sufficient in the middle of the ABL. A linear fit weighted by optical depth std dev including aerosols and cloud returns is displayed (solid line): $\tau = \alpha.z + \varepsilon$, $\varepsilon = -0.09 \pm 0.05$, $\alpha = 1.06 \pm 0.05$ km^{-1}. (b) As in (a), but for 1405 UTC: the aerosol loading is sufficient in the entire ABL. The slope method that relies on aerosol backscatter is plotted as open circles with corresponding std dev. A linear fit weighted by optical depth std dev (error bars) is displayed (dashed line): $\tau = \alpha.z + \varepsilon$, $\varepsilon = 0.04 \pm 0.02$, and $\alpha = 1.01 \pm 0.03$ km^{-1}. A linear fit weighted by optical depth std dev including aerosols and cloud returns is also displayed (solid line): $\tau = \alpha.z + \varepsilon$, $\varepsilon = 0.01 \pm 0.02$, and $\alpha = 1.05 \pm 0.02$ km^{-1}.

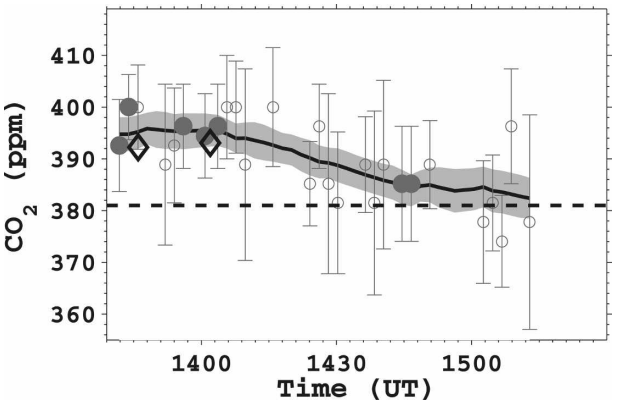

FIG. 12. Experimental results on 26 Mar 2004. The HDIAL CO_2 mixing ratio measurements are displayed when range-distributed aerosol signals are sufficient in the entire ABL (full circle and Fig. 11b) and when it is not the case (empty circle and Fig. 11a). The minimal time resolution is 2 min (600-shot-pair averaging; circle). The solid line corresponds to a 15-min sliding averaging over all 2-min measurements. The std dev for 15 min of time averaging is indicated by the gray area. In situ measurements (diamonds; time resolution of 15 min) stopped at 1430 UTC because of a maintenance problem. Free troposphere (dashed line) measurements are displayed for comparison.

altitude is equal to the ABL height, that is, 1.7 km. On Fig. 11b, the slope or mean CO_2 absorption coefficient is equal to 1.01 ± 0.03 km^{-1}. The optical depth measured using dense cloud returns is 1.63 ± 0.04 for $z = 1.54$ km (see the stars on Fig. 11b). The corresponding mean CO_2 absorption coefficient, 1.06 ± 0.03 km^{-1}, is in a good agreement (5%) with the result of the slope method. Accordingly, the two sets of data can be plotted indistinctly on the same graph as displayed on Fig. 11b. In the case where the aerosol content is not sufficient in some part of the convective ABL, it would enable us to measure the mean extinction coefficient on a longer range for better accuracy (Fig. 11a).

The weighting function is computed using the MM5 model analysis. The PAC information indicated that the laser line was located at the center of the CO_2 P12 absorption line. The HDIAL and in situ CO_2 mixing ratio between 1330 and 1530 UTC are displayed on Fig. 12. Figure 12 considers indistinctly return signals from range-distributed aerosols and cumulus cloud targets. The statistical error for the slope method is 10.6 ppm for a 600-shot-pair averaging (2 min; circles on Fig. 12). The measured standard deviation on CO_2 mixing ratio is 8.2 ppm. A sliding averaging over 15 min (~6-point sliding averaging) decreases the statistical error to 4 ppm or less (gray blurred area). A 15-min slide averaging corresponds to the sampling time reported for in situ data (diamonds on Fig. 12). Unfortunately, in situ measurements stopped at 1430 UTC because of the maintenance of the instrument. However, HDIAL and in situ measurements are in good agreement until this time.

6. HDIAL measurements in the troposphere

a. Results on 5 November 2004: Mean CO_2 mixing ratio in the ABL

Vertical measurements were conducted on 5 November 2004 (or N05 case) during two periods of time around 1000 and 1800 UTC. Figure 13 shows the offline backscatter signal and the vertical velocities. Unfortunately, on this day the HDIAL was not reliable at 1400 UTC and the laser transmitter required several adjustments. This explains the gap between 1400 and 1630 UTC. The N05 case is characterized by winter meteo-

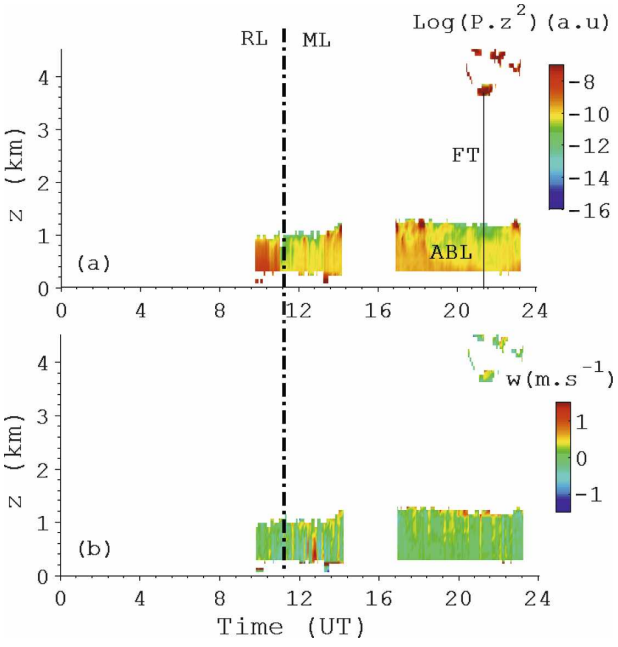

FIG. 13. 5 Nov 2004. Time–height color plots of (a) offline backscatter signal and (b) vertical velocity measured by HDIAL. In (a) color plot is for $\ln(\langle P \rangle z^2)$ in arbitrary unit (red is for the strongest return signals). In (b) positive velocity (red) is upward. Range and time resolution are, respectively, 75 m and 3 min. Solar time is UTC time and LT is UTC time + 1 h.

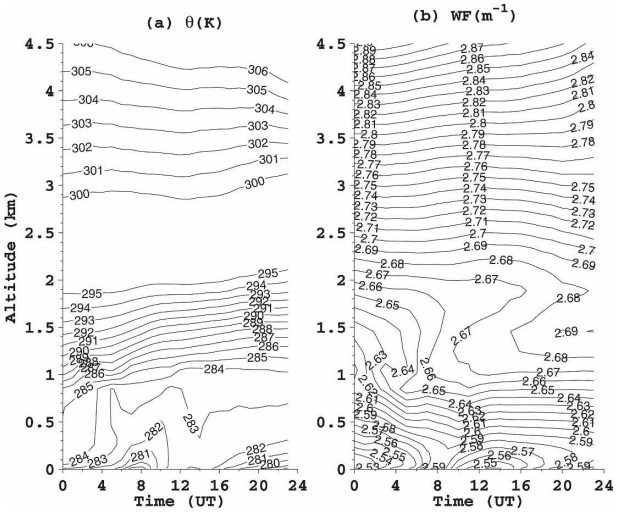

FIG. 14. 5 Nov 2004. Time series of (a) the potential temperature profiles θ (K) from MM5 analysis and (b) calculated weighting function profiles WF (m^{-1}) using spectroscopic data from Table 2 and MM5 outputs for temperature, pressure, and specific humidity. Solar time is UTC time and LT is UTC time + 1 h.

rological conditions, that is, short day time and low temperature (see Fig. 3). This entailed a weak and late development of the ABL. Stratocumulus clouds occur around 1400 UTC and remain present during the night. These observations are consistent with the vertical velocities ($|w| < 0.5$ m s^{-1}) that are recorded in the evening.

At 1000 UTC the HDIAL probes the RL during one hour until 1100 UTC, and then it probes the mixed layer (ML). The RL –ML transition is indicated by the changes in θ and WF contour plots (Fig. 14) and also by the HDIAL vertical velocities measurements.

The on- and offline CNRs are displayed on Fig. 15a, for an accumulation on $M_{p,i} = 900$ shots (i.e., 3-min time averaging). The different noise levels and CNRs at short range are due to different heterodyne efficiencies. The ABL height is ~1 km, which limits the range of application of the slope method. A least square fit weighted by the standard deviation on individual optical depth (corrected from statistical bias) is performed. As for the J10 case, the measured and calculated standard deviations of power estimate are in good agreement. A minimum error on optical depth is obtained for $z \sim 800$ m. Large errors in optical depth are obtained 1) at short range because of small differences in on-and offline signals due to weak absorption 2) at longer range because of weak online SNR. The resulting relative error on the retrieved slope is ~4%. In the ABL, the calculated statistical bias on optical depth (Fig. 15d) is weak and nearly constant with height be-

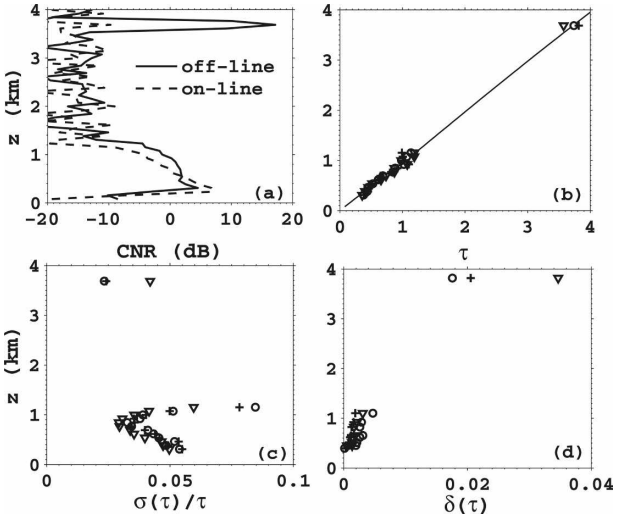

FIG. 15. HDIAL measurements on 5 Nov 2004 at 2130 UTC. (a) Online (dashed curve) and offline (solid curve) CNRs as a function of altitude for 900-shot-pair averaging (3 min) and 75-m range resolution. (b) Three optical depth profiles with 3 min of time averaging are used to retrieve the mean CO_2 mixing ratio in the free troposphere (cross, triangle, and circle). Fit of the measurements using an averaged CO_2 mixing ratio of 405 ppm in the ABL and a free-tropospheric CO_2 mixing ratio $\bar{\rho}_{CO_2}$, $t = 375$ ppm. (c), (d) Relative error and statistical bias on optical depth estimates using the Levin-like estimator for the three optical depth profiles considered, respectively.

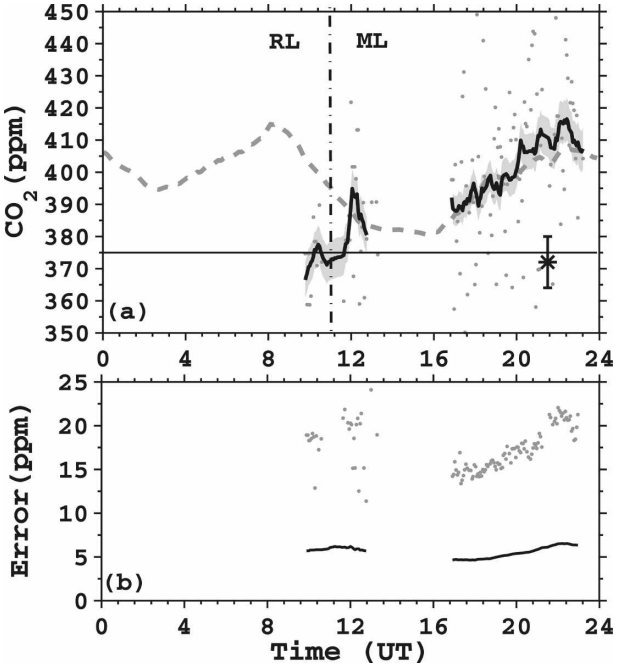

FIG. 16. 5 Nov 2004. (a) CO_2 mixing ratio as measured by the 2-μm HDIAL pointing vertically for 900-shot-pair averaging or 3 min (gray dots) and 10-point sliding averaging or 30-min averaging (black thick solid line) and LSCE in situ routine measurements (gray dashed line). The gray blurred area corresponds to the standard deviation of the 30-min averaged measurements. Mean CO_2 mixing ratio measurements in the free troposphere are indicated for the routine airborne in situ measurements (thin solid line) and for the HDIAL retrievals (star). (b) Statistical relative error on HDIAL CO_2 measurements associated to the slope method for 3-min averaging (gray dots) and 10-point sliding averaging or 30-min averaging (black solid line). Solar time is UTC time and local time is UTC time + 1 h.

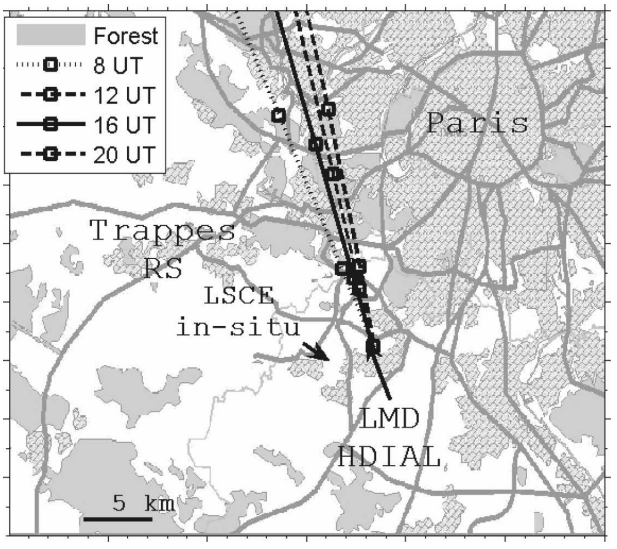

FIG. 17. 5 Nov 2004. NCEP 800-m-height back trajectories at different times of the day. The time interval (sampling) between two squares along the same trajectory is 1 h.

cause of similar on- and offline CNRs in the ABL and because of a large number of shot-pair averaging.

Here WF was calculated from MM5 model outputs as. Figure 16a displays the vertical HDIAL measurements to be compared to in situ CO_2 mixing ratio measurements. The temporal resolution is 3 min (points). A 10-point sliding average (or 30-min solid line in Fig. 16a) decreases the statistical error to 5 ppm or less (see the gray blurry area). On 5 November 2004, the PAC signals show a quite stable behavior of the HDIAL system during the whole experiment.

In winter, several factors contribute to an increase of CO_2 density near the surface 1) energy and fuel combustions and 2) shallow ABL. Between 0930 and 1100 UTC, for the HDIAL measurements are conducted mostly in the RL (see Figs. 14, 16), the 375 ± 3 ppm value are in good agreement with the values observed in the ML and significant differences occur between HDIAL and in situ ground-based measurements taken in the NL. After 1100 UTC, the HDIAL and in situ measurements probe the same mixed layer and so are in good agreement, within 5 ppm (it is also a clear indication that the two locations are in the same air mass).

During the evening, when the air mass is coming from the north (Fig. 17), some vertical mixing processes still occurred associated to stratocumulus cloud activity (Fig. 13). During this period, the HDIAL and in situ measurements agree quite well, even if the HDIAL measurements are slightly larger than in situ measurements by ~7 ppm after 2000 UTC. These discrepancies can be associated with the location of each site and a weak vertical mixing. Given the horizontal wind direction at 800-m height (Fig. 13), the LMD site is located at the edge of the Paris urban area and is therefore more sensitive to anthropogenic emissions.

b. HDIAL CO_2 mixing ratio measurements in the free troposphere using midaltitude clouds

On 5 November 2004, the HDIAL was pointing at zenith to a midtropospheric cloud at an altitude of 3.7 km. Few measurements were available at 2130 UTC (Figs. 13, 15). From these measurements, we retrieve the CO_2 mixing ratio in the free troposphere by a difference between the path-integrated CO_2 measurement to the cloud base and the slope method in the ABL.

The mean CO_2 mixing ratio in the ABL is $\bar{\rho}_{CO_2}$, a = 405 ± 5 ppm (Fig. 16). Despite the fact that the optical depth to the cloud base is large $\tau(0, 3.7) = 3.75$ (Fig. 15b), no optimization of the online absorption has been made in this preliminary study. As a consequence, the

low CNR requires an averaging on a large number of pulse pairs to obtain a sufficient SNR. It is worth noticing that the signal dynamic in heterodyne detection applies to signal amplitude that is the square root of the signal dynamic in direct detection. It can be considered an important advantage. It is, however, true that, for such a long path-integrated measurement using the same CO_2 P12 line, a stabilization device to detune accurately off line center the online emission would improve the statistical error and the time resolution.

Now, starting from the ABL top, we conducted a parametric study using various $\bar{\rho}_{CO_2}$, t values to fit the measurements made using the cloud base as a target. Such a fitting enables us to derive a CO_2 mixing ratio in the free troposphere (Figs. 15, 16). The best fit is obtained for $\bar{\rho}_{CO_2}$, $t = 372 \pm 8$ ppm, while airborne measurements report 375.0 ± 0.5 ppm in the free troposphere, 100 km south of Paris. It is worth noting that the tropospheric CO_2 mixing ratio is quite stable in time and space over several days and hundreds of kilometers without meteorological synoptic change. The ± 8 ppm on the HDIAL measurements are calculated as a total error including statistical and weighting function errors and considered an average over the three measurements that were available. The amplitude of the annual and monthly variations of free-tropospheric CO_2 in the Northern Hemisphere is 10 ppm and less than 2 ppm, respectively (Bakwin et al. 1998; Gibert et al. 2007c). Assuming a higher number of measurements per month to decrease the statistical error, the HDIAL system has the potential to monitor the mean free-tropospheric CO_2 mixing ratio.

7. Conclusions

Vertical CO_2 density measurements in the atmospheric boundary layer performed by a 2-μm heterodyne DIAL system have been validated. When the representativity error is minimized according to the meteorological conditions the HDIAL measurements are in good agreement with contemporary in situ data. The slope method results in accurate mean CO_2 density provided that the weighting function is computed with sufficient accuracy. We have used the new spectroscopic data that have been made available recently for the absorption cross section of the CO_2 P12 online. A photo acoustic cell device enables us to correct efficiently for frequency drift that occurs during the course of the measurements. The effective ABL height sets a limit on range for an application of the slope method that in turn results in less accuracy. On 5 November 2004, where the ABL height is ~1 km, the accuracy is 4% (or 15–20 ppm) for an averaging over 900 shot pairs or 3 min. A 10-point sliding averaging (over 30 min) decreases the absolute error to 5 ppm. On 10 June 2005, according to the ABL diurnal cycle, CO_2 measurements were made in the NL, RL, and ML. When pointing horizontally in the NL, in situ and HDIAL measurements agree within 1%. Although the ABL height reaches ~2 km in the midafternoon, a strong decrease of aerosol backscatter signal with altitude limits the range of HDIAL measurements to ~1.2 km. An accumulation over 30 min is necessary to decrease the error to ~6 ppm. The resulting 30 min is due to a limited 5-Hz PRF. Increasing the PRF by an order of magnitude would shorten the accumulation time to a few minutes for the same accuracy.

The HDIAL measurements were conducted looking vertically in the atmospheric boundary layer using aerosol backscatter as well as dense cloud returns when cumulus clouds were present at the top of the ABL. The two methods were compared successfully and also with ground-based in situ measurements in the mixed layer. The accuracy is ~10–15 ppm for 600-shot-pair averaging (or 2 min) and ~4 ppm for 15 min where the ABL height is ~1.8 km. Dense clouds at the top of the ABL enable us to overcome the limitation due to low aerosol burden in some parts of the ABL. Midaltitude clouds were also used to conduct preliminary measurements of the mean CO_2 mixing ratio in the free troposphere. On one day the retrieved value 372 ± 8 ppm by HDIAL agrees with in situ airborne measurements, that is, 375 ± 0.5 ppm, made ~100 km away, whereas the ABL mixing ratio calculated with the slope method amounted to 405 ± 5 ppm.

Acknowledgments. The instrument development and testing has been supported by Centre National d'Etudes Spatiales (CNES) and Institut Pierre-Simon Laplace (IPSL). The authors are thankful to M. Ramonet, M. Schmidt and the RAMCES team from LSCE/IPSL who provided the in situ CO_2 measurements for comparison and validation. We also thank Kenneth J. Davis for his comments and suggestions.

APPENDIX A

Errors Induced by the Spectral Dependence of Aerosol Optical Properties

Using the simplified lidar equation, the atmospheric scattered power in a range gate ΔR at range R is

$$\langle P_i(R)\rangle = \frac{K_i}{R^2} E_i \langle \gamma_i(R)\rangle \langle \beta_{p,i}(R)\rangle \exp\left\{-2\int_0^R [\alpha_i(r) + \alpha_{p,i}(r)]\, dr\right\}, \quad \text{(A1)}$$

where K_i is a instrumental constant for the wavelength i, E_i is the pulse energy, γ_i is the heterodyne efficiency, $\beta_{p,i}$ is the particle backscatter coefficient (m sr^{-1}), α_i is the CO_2 absorption (m^{-1}), and $\alpha_{p,i}$ is the particle extinction coefficient (m^{-1}).

Assuming the same heterodyne efficiency range dependence for the two wavelengths (i.e., $\gamma_{\mathrm{Off}}(r)/\gamma_{\mathrm{On}}(r) = C^{te}$, which is easily checked tuning the online LO wavelength toward the offline wavelength) and using Eq. (A1), we retrieve the CO_2 differential absorption α:

$$\alpha = \frac{d}{dR}\left[\frac{1}{2}\ln\left(\frac{\langle P_{\mathrm{Off}}\rangle}{\langle P_{\mathrm{On}}\rangle}\right)\right] + \frac{d}{dR}\left[\frac{1}{2}\ln\left(\frac{\langle \beta_{p,\mathrm{Off}}\rangle}{\langle \beta_{p,\mathrm{On}}\rangle}\right)\right] + \alpha_{p,\mathrm{Off}} - \alpha_{p,\mathrm{On}}. \quad \text{(A2)}$$

The bias induced by aerosols' optical properties depends on (i) the difference of aerosol optical depth between the two wavelengths and (ii) the changes of aerosol intensive optical properties (i.e., refractive index, size, and shape) within the CO_2 retrieval range, which modify spectral dependence of the backscatter coefficient. To evaluate this bias, numerical simulations using a Mie scattering code for homogeneous spherical particles (Mätzler 2002) and accounting for the relative humidity have been performed.

Accounting for particle size, complex refractive index, and RH vertical gradient, we may express the particle extinction $\alpha_{p,i}$ and backscatter $\beta_{p,i}$ coefficients as follows (D'Almeida et al. 1991):

$$\alpha_{p,i}(\lambda_i, \mathrm{RH}) = \int_0^\infty \pi {r_{\mathrm{RH}}}^2 Q_{\mathrm{ext}}[2\pi r_{\mathrm{RH}}/\lambda_i, n_{\mathrm{RH}}(\lambda_i)] \frac{dN}{d\log r}(r_{\mathrm{RH}})\, d\log r, \quad \text{(A3)}$$

$$\beta_{p,i}(\lambda_i, \mathrm{RH}) = \int_0^\infty \pi {r_{\mathrm{RH}}}^2 Q_{\mathrm{back}}[2\pi r_{\mathrm{RH}}/\lambda_i, n_{\mathrm{RH}}(\lambda_i)] \frac{dN}{d\log r}(r_{\mathrm{RH}})\, d\log r, \quad \text{(A4)}$$

where λ_i is the probing wavelength, r is the particle radius, the subindex RH indicates the dependence with relative humidity RH, Q_{ext} and Q_{back} are the extinction and backscatter efficiency computed as a function of the size parameter $2\pi r/\lambda_i$ and complex refractive index $n(\lambda_i)$, and $dN/d\log r$ is the particle number size distribution (dN represents the number of particles per unit volume of air with a radius between r and $r + dr$).

Here $dN/d\log r$ is computed using column-integrated volume size distribution $dV/d\ln r$ retrieved by a sun photometer operated on the same site (see Holben et al. 1998; Dubovik and King 2000). Figure A1a shows three different size distributions in cloud-free atmosphere and in the absence of FT aerosol layers (the case of 10 June 2005 was unfortunately not available; see Gibert et al. 2007a). To deal with a practical $dN/d\log r$ profile in the CBL, we consider a uniform number distribution between ground level and z_i, as well as a negligible contribution from the FT. Then we use

$$\frac{dN}{d\log r}(r) = \frac{1}{(4/3)\pi r^3 \ln(10)} \frac{1}{z_i} \frac{dV}{d\ln r}(r). \quad \text{(A5)}$$

The complex index of refraction n(λ) corresponds to the values compiled in D'Almeida et al. (1991) for water-soluble aerosols—a major component of urban aerosols in terms of volume concentration—linearly interpolated for the lidar wavelengths. Furthermore, the parameterization used to account for relative humidity effects on size and complex index of refraction n(z) is the following (Hänel 1976):

$$r_{\mathrm{RH}} = r_1 \left[\frac{1 - \mathrm{RH}(z)/100}{1 - \mathrm{RH}_1/100}\right]^{-\varepsilon}, \quad \text{(A6)}$$

$$n_{\mathrm{RH}} = n_W + (n_0 - n_W)\left(\frac{r_0}{r_{\mathrm{RH}}}\right)^3, \quad \text{(A7)}$$

where RH(z) is the relative humidity profile measured by radiosounding; RH_1 is a reference relative humidity, which is here considered as the mean value over the CBL; the mean radius r_1 is approximated by the one retrieved by the "Almucantar" inversion (Dubovik and King 2000); r_0 is the dry particle radius obtained from Eq. (A6) for RH = 0; and n_0 and n_w are the dry particle and water index of refraction (D'Almeida et al. 1991). The exponent ε depends on the hygroscopic degree of the particles. We use $\varepsilon = 0.26$ for the Paris area (Randriamiarisoa et al. 2005). The RH profiles at 1130 UTC show a linear increase of RH from nearly 40% at the surface to 70% at CBL top for the three cases investigated.

Figures A1b,c display the numerical simulations of the bias induced by aerosols optical properties accounting for backscatter and extinction coefficients, respectively.

APPENDIX B

Weighting Function

Using the slope method, the CO_2 mixing ratio is given by

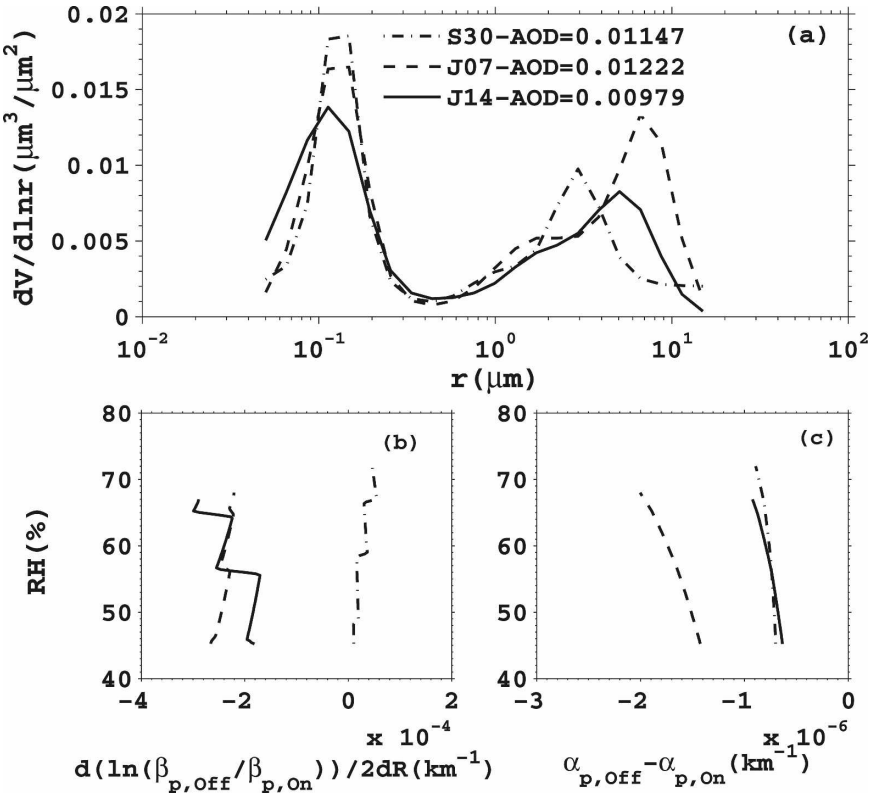

FIG. A1. (a) Size distributions retrieved by a sun photometer collocated with the HDIAL at LMD/IPSL for the cases 30 Sep 2003 (S30), 7 Jun 2004 (J07), and 14 Jun 2005 (J14) (solid, dashed, and dashed–dotted lines, respectively). (b), (c) Bias on CO_2 differential absorption measurement accounting for backscatter and extinction, respectively. AOD is the calculated aerosol optical depth at 2.064 nm.

$$\rho_{CO_2}(z) = \frac{1}{\mathrm{WF}(z)} \frac{d\tau(0, z)}{dz}, \tag{B1}$$

where $\mathrm{WF}(z)$ is a weighting function and $\tau(0, z)$ is the optical depth. From Eq. (B1) [Eq. (8) in the main text], it is clear that a systematic error can be caused either by an error on the first derivative of the optical depth or the weighting function. For the i line, WF_i is given by

$$\mathrm{WF}_i = n_a \tilde{\sigma}_i, \tag{B2}$$

where $\tilde{\sigma}_i$ is the i-line absorption cross section and

$$n_a(z) = \frac{p(z)}{kT(z)} \frac{1}{1 + \rho_w(z)}, \tag{B3}$$

where ρ_w is the water vapor mixing ratio, p is the pressure, T is the temperature, and k is the Boltzmann constant.

We analyze the WF sensitivity to random–systematic errors on pressure, temperature, and humidity profiles. We assume a Lorentzian shape for the P12 CO_2 absorption line cross section:

$$\tilde{\sigma}_i = \frac{S}{\pi\gamma} \frac{1}{1 + (\Delta\tilde{\upsilon}/\gamma)^2}, \tag{B4}$$

where $\Delta\tilde{\upsilon} = (\upsilon - \upsilon_0)/c$ is the detuning from line center in wavenumber and S is the line intensity:

$$S = S_0 \left(\frac{T_0}{T}\right) \exp\left[-\frac{E''hc}{k}\left(\frac{1}{T} - \frac{1}{T_0}\right)\right], \tag{B5}$$

where E'' is the energy of the lower level of the transition; h is the Planck constant; c is the light velocity; γ is the half-width at half-maximum (HWHM):

$$\gamma = \gamma_0 \frac{p}{p_0} \left(\frac{T_0}{T}\right)^t; \tag{B6}$$

S_0 and γ_0 are the intensity and HWHM for the standard pressure p_0 and temperature T_0, respectively; and t is the coefficient for temperature dependence (see Table 2).

Using Eqs. (B2)–(B6), we obtain

$$\mathrm{WF}_i(\rho_w, T, p) = n_0\tilde{\sigma}_0 \frac{1}{1+\rho_w}\left(\frac{T_0}{T}\right)^{2-t} \exp\left[-\frac{E''hc}{k}\left(\frac{1}{T}-\frac{1}{T_0}\right)\right]\frac{1}{1+[\Delta\tilde{\nu}/\gamma(T,p)]^2}. \quad \text{(B7)}$$

Using Eq. (B7), an error on the humidity profile entails an error:

$$\frac{\sigma(\mathrm{WF}_i)}{\mathrm{WF}_i} = -\frac{\rho_w}{1+\rho_w}\frac{\sigma(\rho_w)}{\rho_w}. \quad \text{(B8)}$$

Assuming a specific humidity of $\rho_w = 10 \pm 1$ g kg^{-1}, the resulting error on the weighting function is only 0.1%. Notice that 10 g kg^{-1} is quite large at midlatitude.

The sensitivity of the weighting function to pressure needs to be considered when the transmitter line is detuned from the P12 line center [Eq. (B7)]. The pertinent parameter to be considered is the surface pressure. The relative error on weighting function due to the surface pressure is

$$\frac{\sigma(\mathrm{WF}_i)}{\mathrm{WF}_i} = -2\frac{(\Delta\tilde{\nu}/\gamma)^2}{1+(\Delta\tilde{\nu}/\gamma)^2}\frac{\sigma(P_{\mathrm{surf}})}{P_{\mathrm{surf}}}. \quad \text{(B9)}$$

Assuming $P = P_0$, a 1-hPa error on surface pressure entails a ~0.1% relative error on the weighting function for a detuning equal to γ_0 from the CO2 P12 line center.

From Eq. (B7), the relative error on WF_i due to a temperature error is

$$\frac{\sigma(\mathrm{WF}_i)}{\mathrm{WF}_i} = -\left[\frac{E''hc}{kT} - 2 - t\frac{(\Delta\tilde{\nu}/\gamma)^2-1}{(\Delta\tilde{\nu}/\gamma)^2+1}\right]\frac{\sigma(T)}{T}. \quad \text{(B10)}$$

An optimal condition can be reached for a given spectral detuning from absorption line center:

$$E''_{\mathrm{opt}} = \frac{kT}{hc}\left[2 + t\frac{(\Delta\tilde{\nu}/\gamma)^2-1}{(\Delta\tilde{\nu}/\gamma)^2+1}\right]. \quad \text{(B11)}$$

However, the energy of the lower transition of the CO_2 P12 line is too low to reach this optimum (i.e., $E''_{\mathrm{opt}} = 250$ cm^{-1} for $T = T_0$ and $\Delta\tilde{\nu}/\gamma = 0$). Therefore, assuming $T = T_0$, the resulting error on the weighted function for a 1-K temperature uncertainty amounts to 0.4% and is lower than 0.8% whatever the detuning from the CO_2 P12 line center is.

APPENDIX C

Bias on Optical Depth Estimate

The optical depth, for a single shot pair and range gate is

$$\tilde{\tau}(0,z) = \frac{1}{2}\ln\left[\frac{\langle P_{\mathrm{off}}(z)\rangle}{\langle P_{\mathrm{on}}(z)\rangle}\right]. \quad \text{(C1)}$$

On and off signals are made of a useful component denoted $\overline{\langle P_{\mathrm{off/on}}\rangle}$ for time accumulation and a noise contribution $p_{\mathrm{off/on}}$:

$$\langle P_{\mathrm{off/on}}\rangle = \overline{\langle P_{\mathrm{off/on}}\rangle} + p_{\mathrm{off/on}}. \quad \text{(C2)}$$

Then, from (C1), one obtains

$$2\tilde{\tau} = \ln\left(\frac{\overline{\langle P_{\mathrm{off}}\rangle}}{\overline{\langle P_{\mathrm{on}}\rangle}}\right) + \ln\left(1+\frac{p_{\mathrm{off}}}{\overline{\langle P_{\mathrm{off}}\rangle}}\right) - \ln\left(1+\frac{p_{\mathrm{on}}}{\overline{\langle P_{\mathrm{on}}\rangle}}\right). \quad \text{(C3)}$$

Assuming that the fluctuations are weak compared to the useful component $(p_{\mathrm{off/on}}/\overline{\langle P_{\mathrm{off/on}}\rangle}) \ll 1$,

$$2\tilde{\tau} = \ln\left(\frac{\overline{\langle P_{\mathrm{off}}\rangle}}{\overline{\langle P_{\mathrm{on}}\rangle}}\right) + \frac{p_{\mathrm{off}}}{\overline{\langle P_{\mathrm{off}}\rangle}} - \frac{p_{\mathrm{on}}}{\overline{\langle P_{\mathrm{on}}\rangle}} - \frac{1}{2}\left(\frac{p_{\mathrm{off}}}{\overline{\langle P_{\mathrm{off}}\rangle}}\right)^2 + \frac{1}{2}\left(\frac{p_{\mathrm{on}}}{\overline{\langle P_{\mathrm{on}}\rangle}}\right)^2. \quad \text{(C4)}$$

After shot pairs and range gate accumulation, then $\langle(p_{\mathrm{off}}/\overline{\langle P_{\mathrm{off}}\rangle}) - (p_{\mathrm{on}}/\overline{\langle P_{\mathrm{on}}\rangle})\rangle \approx 0$ and the useful mean optical depth is

$$\tilde{\tau} = \tau + \frac{1}{4}\left[\frac{1}{\mathrm{SNR}^2_{\mathrm{on}}} - \frac{1}{\mathrm{SNR}^2_{\mathrm{off}}}\right], \quad \text{(C5)}$$

where $\tau = \frac{1}{2}\ln(\overline{\langle P_{\mathrm{off}}\rangle}/\overline{\langle P_{\mathrm{on}}\rangle})$ is an estimate of the optical depth biased by time accumulation. When the SNR is weak, the calculated optical depth is underestimated. However, the bias is negligible for comparable high SNR*s* for the on- and offline signals accounting for a large number of shot pairs or range gate averaging (SNR>10) that is currently the case for our DIAL measurements.

APPENDIX D

Digitizing Noise

The heterodyne amplitude voltage is digitized on 8 bits at a 125-MHz sampling frequency. One can write

$$S_i = n\mathrm{LSB}, \quad \text{(D1)}$$

where the LSB is the least significant bit. It corresponds to an uncertainty on the signal and is the digitizing

noise. Assuming that the probability p that the signal be between $(n - 1/2)$LSB and $(n + 1/2)$LSB is uniform, we obtain $p(S_i) = 1/\text{LSB}$, and the heterodyne signal digitizing noise variance is

$$\int_{(n-1/2)\text{LSB}}^{(n+1/2)\text{LSB}} S_i^2 p(S_i)\, dS_i - \left[\int_{(n-1/2)\text{LSB}}^{(n+1/2)\text{LSB}} S_i p(S_i)\, dS_i\right]^2 = \left[\frac{S_i^3}{3\text{LSB}} - \left(\frac{S_i^2}{2\text{LSB}}\right)^2\right]_{(n-1/2)\text{LSB}}^{(n+1/2)\text{LSB}} = \text{LSB}^2/12. \quad \text{(D2)}$$

In heterodyne detection, the optical power is proportional to the squared amplitude voltage S_i. Therefore, we have $dP_i/P_i = 2dS_i/S_i$ and finally we obtain the digitizing noise on the optical return power $\sigma^2(P_i) = \text{LSB}^2 P_i/3$. For an average return signal over Mp shots in a 75-m range gate, we obtain

$$\frac{\sigma(\overline{\langle P_i \rangle})}{\overline{\langle P_i \rangle}} = \sqrt{\frac{c}{2 f_S \Delta R}} \frac{\text{LSB}}{\sqrt{3 P_i}}, \quad \text{(D3)}$$

where f_S is the sampling frequency (i.e., 125 MHz), c is the light velocity, and ΔR is the range gate (i.e., 75 m).

REFERENCES

Bakwin, P. S., P. P. Tans, D. F. Hurst, and C. Zhao, 1998: Measurements of carbon dioxide on very tall towers: Results of the NOAA/CMDL program. *Tellus,* **50B,** 401–415.

——, ——, B. B. Stephens, S. C. Wofsy, C. Gerbig, and A. Grainger, 2003: Strategies for measurement of atmospheric column means of carbon dioxide from aircraft using discrete sampling. *J. Geophys. Res.,* **108,** 4514, doi:10.1029/2002JD003306.

Braud, H., P. Bousquet, M. Ramonet, R. Sarda, and P. Ciais, 2004: CO/CO_2 ratio in urban atmosphere: Example of the agglomeration of Paris, France. Institut Pierre et Simon Laplace Notes des Activités Instrumentales 42, 11 pp.

Bruneau, D., O. Le Rille, J. Pelon, and P. H. Flamant, 1997: Development of 2-μm coherent lidar emitter with transform-limited pulse output for wind and water-vapor measurements. *Proc. Ninth Coherent Laser Radar Conf.,* Linköping, Sweden, Swedish Defence Research Establishment (FOA), 54–57.

——, S. Delmonte, and J. Pelon, 2000: Wind velocity and backscatter measurements at 2-μm with the heterodyne detection lidar EMIL. *Proc. 20th Int. Laser Radar Conf.,* Vichy, France, École Polytechnique, 97–100.

——, F. Gibert, P. H. Flamant, and J. Pelon, 2006: A complementary study of DIAL optimization in direct and heterodyne detections. *Appl. Opt.,* **45,** 4898–4908.

Conway, T. J., P. P. Tans, L. S. Waterman, and K. W. Thoning, 1994: Evidence for interannual variability of the carbon cycle from the National Oceanic and Atmospheric Administration Climate Monitoring and Diagnostics Laboratory Global Air-Sampling Network. *J. Geophys. Res.,* **99** (D11), 22 831–22 855.

Crisp, D., and Coauthors, 2004: The Orbiting Carbon Observatory (OCO) mission. *Adv. Space Res.,* **34,** 700–709.

D'Almeida, G. A., P. Koepke, and E. P. Shettle, Eds., 1991: *Atmospheric Aerosols: Global Climatology and Radiative Characteristics.* A. Deepak, 561 pp.

Dubovik, O., and M. D. King, 2000: A flexible inversion algorithm for retrieval of aerosol optical properties from Sun and sky radiance measurements. *J. Geophys. Res.,* **105,** 20 673–20 696.

Flamant, P. H., and Coauthors, 2005: FACTS: Future Atmospheric Carbon dioxide Testing from Space. European Space Agency Final Rep. 1/3, 223 pp.

Gibert, F., P. H. Flamant, D. Bruneau, and C. Loth, 2006: 2-μm heterodyne differential absorption lidar measurements of atmospheric CO_2 mixing ratio in the boundary layer. *Appl. Opt.,* **45,** 4448–4458.

——, J. Cuesta, J.-I. Yano, N. Arnault, and P. H. Flamant, 2007a: On the correlation between convective plume updrafts and downdrafts, lidar reflectivity and depolarization ratio. *Bound.-Layer Meteor.,* **125,** 575–578.

——, F. Marnas, D. Edouart, and P. H. Flamant, 2007b: An a posteriori method based on photo-acoustic cell information to correct for lidar transmitter spectral shift. Application to atmospheric CO_2 DIAL measurements. *Appl. Spectrosc.,* **61,** 1068–1075.

——, M. Schmidt, J. Cuesta, E. Larmanou, M. Ramonet, P. H. Flamant, I. Xueref, and P. Ciais, 2007c: Retrieval of average CO_2 fluxes by combining in-situ CO_2 measurements and backscatter lidar information. *J. Geophys. Res.,* **112,** D10301, doi:10.1029/2006JD008190.

Grell, G. A., J. Dudhia, and D. R. Stauffer, 1995: A description of the fifth-generation Penn State/NCAR mesoscale model (MM5). NCAR Tech. Note, NCAR/TN-398+STR, 121 pp.

Hänel, G., 1976: The properties of atmospheric aerosol particles as functions of the relative humidity at the thermodynamic equilibrium with the surrounding moist air. *Advances in Geophysics,* Vol. 19, Academic Press, 73–188.

Henderson, S. W., E. Y. Yuen, and E. S. Fry, 1986: Fast resonance detection technique for single-frequency operation of injection seeded Nd:YAG lasers. *Opt. Lett.,* **11,** 715–717.

Holben, B. N., and Coauthors, 1998: AERONET—A federated instrument network and data archive for aerosol characterization. *Remote Sens. Environ.,* **66,** 1–16.

Houghton, J. T., Y. Ding, D. J. Griggs, M. Noguer, P. J. van der Linden, X. Dai, K. Maskell, and C. A. Johnson, Eds., 2001: *Climate Change 2001: The Scientific Basis.* Cambridge University Press, 881 pp.

Hurwitz, M. D., D. M. Ricciuto, P. S. Bakwin, K. J. Davis, W. Wang, C. Yi, and M. P. Butler, 2004: Transport of carbon dioxide in the presence of storm system over a northern Wisconsin forest. *J. Atmos. Sci.,* **61,** 607–618.

Idso, S. B., C. D. Idso, and R. C. Balling Jr., 2002: Seasonal and diurnal variations of near-surface atmospheric CO_2 concentration within a residential sector of the urban CO_2 dome of Phoenix, AZ, USA. *Atmos. Environ.,* **36,** 1655–1660.

Inoue, G., 2005: The greenhouse gases monitoring *in-situ* and from space (GOSAT). *Proc. 13th Coherent Laser Radar Conf.,* Kamakura, Japan, National Institute of Information and Communications Technology, 101–104.

Killinger, D. K., and N. Menyuk, 1981: Remote probing of the

atmosphere using a CO_2 DIAL system. *IEEE J. Quantum Electron.,* **9,** 1917–1929.

Koch, G. J., and Coauthors, 2004: Coherent differential absorption lidar measurements of CO_2. *Appl. Opt.,* **43,** 5092–5099.

Lambert, G., P. Monfray, B. Ardouin, G. Bonsang, A. Gaudry, V. Kazan, and G. Polian, 1995: Year-to-year changes in atmospheric CO_2. *Tellus,* **47B,** 53–55.

Liou, K.-N., 1981: Some aspects of the optical properties of ice clouds. *Clouds: Their Formation, Optical Properties, and Effects,* P. V. Hobbs and A. Deepak, Eds., Academic Press, 497 pp.

Lloyd, J., and Coauthors, 2001: Vertical profiles, boundary layer budgets, and regional flux estimates for CO_2 and its $^{13}C/^{12}C$ ratio and for water vapour above a forest/bog mosaic in central Siberia. *Global Biogeochem. Cycles,* **15,** 267–284.

Matsueda, H., and H. Inoue, 1996: Measurements of atmospheric CO_2 and CH_4 using a commercial airliner from 1993 to 1994. *Atmos. Environ.,* **30,** 1647–1655.

Mätzler, C., 2002: MATLAB functions for Mie scattering and absorption, version 2. IAP Research Rep., 11 pp.

Megie, G., and R. T. Menzies, 1980: Complementarity of UV and IR differential absorption lidar for global measurements of atmospheric species. *Appl. Opt.,* **19,** 1173.

Pépin, L., M. Schmidt, M. Ramonet, D. Worthy, and P. Ciais, 2002: A new gas chromatographic experiment to analyze greenhouse gases in flask samples and in ambient air in the region of Saclay. Instrumental Notes of IPSL 13, 27 pp.

Randriamiarisoa, H., P. Chazette, P. Couvert, and J. Sanak, 2005: Relative humidity impact on aerosol parameters in a Paris suburban area. *Atmos. Chem. Phys. Discuss.,* **5,** 8091–8147.

Rayner, P. J., and D. M. O'Brien, 2001: The utility of remotely sensed CO2 concentration data in surface source inversions. *Geophys. Res. Lett.,* **28,** 175–178.

Regalia-Jarlot, L., V. Zéninari, B. Parvitte, A. Grossel, X. Thomas, P. von der Heyden, and G. Durry, 2006: A complete study of the line intensities of four bands of CO_2 around 1.6 and 2.0 μm: A comparison between Fourier transform and diode laser measurements. *J. Quant. Spectrosc. Radiat. Transfer,* **101,** 325–338.

Remsberg, E., and L. Gordley, 1978: Analysis of differential absorption lidar from the space shuttle. *Appl. Opt.,* **17,** 624–630.

Rothman, L. S., and Coauthors, 1998: The HITRAN molecular spectroscopic database, and HAWKS (HITRAN Atmospheric Workstation): 1996 edition. *J. Quant. Spectrosc. Radiat. Transfer,* **60,** 665–710.

Rye, B. J., and R. M. Hardesty, 1993: Discrete spectral peak estimation in incoherent backscatter heterodyne lidar. I: Spectral accumulation and the Cramer-Rao lower bound. *IEEE Trans. Geosci. Remote Sens.,* **31,** 16–27.

——, and ——, 1997: Estimate optimization parameters for incoherent backscatter heterodyne lidar. *Appl. Opt.,* **36,** 9425–9436.

Schmitgen, S., P. Ciais, H. Geiss, D. Kley, A. Voz-Thomas, B. Neiniger, M. Baeumle, and Y. Brunet, 2004: Carbon dioxide uptake of a forested region in southwest France derived from airborne CO_2 and CO observations in a Lagrangian budget approach. *J. Geophys. Res.,* **109,** D14302, doi:10.1029/2003JD004335.

Stephens, B. B., and Coauthors, 2007: Weak northern and strong tropical land carbon uptake from vertical profiles of atmospheric CO_2. *Science,* **316,** 1732–1735, doi:10.1126/science.1137004.

Tonna, G., 1991: Backscattering, extinction, and liquid water content in fog: A detailed study of their relations for use in lidar systems. *Appl. Opt.,* **30,** 1132–1140.

Wang, J.-W., A. S. Denning, L. Lu, I. T. Baker, K. D. Corbin and K. J. Davis, 2007: Observations and simulations of synoptic, regional, and local variations in atmospheric CO_2. *J. Geophys. Res.,* **112,** D04108, doi:10.1029/2006JD007410.

Worthy, D. E. J., I. Levin, N. B. A. Trivett, A. J. Kuhlmann, J. F. Hopper, and M. K. Ernst, 1998: Seven years of continuous methane observations at a remote boreal site in Ontario, Canada. *J. Geophys. Res.,* **103** (D13), 15 995–16 007.

Yi, C., K. J. Davis, P. S. Bakwin, A. S. Denning, N. Zhang, A. Desai, J. C. Lin, and C. Gerbig, 2004: Observed covariance between ecosystem carbon exchange and atmospheric boundary layer dynamics at a site in northern Wisconsin. *J. Geophys. Res.,* **109,** D08302, doi:10.1029/2003JD004164.